Title: Ocean Acidification and the Permo-Triassic Mass Extinction

Authors: Clarkson, M.O.[1*]; Kasemann, S.A.[2]; Wood, R.[1]; Lenton, T.M.[3]; Daines, S.J.[3]; Richoz, S.[4]; Ohnemueller, F.[2]; Meixner, A.[2]; Poulton, S.W.[5] and Tipper, E.T.[6]

Affiliations:

[1.] School of Geosciences, University of Edinburgh, West Mains Road, Edinburgh, EH9 3JW, UK

[2.] Faculty of Geosciences and MARUM-Center for Marine Environmental Sciences, University of Bremen, 28334 Bremen, Germany

[3.] College of Life and Environmental Sciences, University of Exeter, Laver Building, North Parks Road, Exeter, EX4 4QE, UK.

[4.] Institute of Earth Sciences, University of Graz, Heinrichstraße 26, 8010 Graz, Austria

[5.] School of Earth and Environment, University of Leeds, Leeds, LS2 9JT, UK

[6.] Dept. of Earth Sciences, University of Cambridge, Downing Street, Cambridge, CB2 3EQ, UK

*Correspondence to: matthew.clarkson@otago.ac.nz

Current address: Department of Chemistry, University of Otago, Union Street, Dunedin, 9016, PO Box 56, New Zealand.

Abstract: Ocean acidification triggered by Siberian Trap volcanism has been implicated as a kill mechanism for the Permo-Triassic mass extinction, but evidence for an acidification event remains inconclusive. To address this, we present a high resolution seawater pH record across this interval, utilizing boron isotope data combined with a quantitative modeling approach. In the latest Permian, the alkalinity of the ocean increased, priming the Earth system with a low level of atmospheric CO_2 and a high ocean buffering capacity. The first phase of extinction was

24   coincident with a slow injection of isotopically light carbon into the atmosphere-ocean, but the

25   ocean was well-buffered such that ocean pH remained stable. During the second extinction pulse,

26   however, a rapid and large injection of carbon overwhelmed the buffering capacity of the ocean,

27   causing an abrupt and short-lived acidification event that drove the preferential loss of heavily

28   calcified marine biota.

29

30   **One Sentence Summary:** Ocean acidification caused the second phase of mass extinction in the

31   Permo-Triassic, due to a rapid and large injection of carbon which overwhelmed the buffering

32   capacity of the ocean.

33

34   **Main Text:** The Permian Triassic Boundary (PTB) mass extinction, at ~ 252 Ma, represents the

35   most catastrophic loss of biodiversity in geological history, and played a major role in dictating

36   the subsequent evolution of modern ecosystems (*1*). The end-Permian extinction event spans ~60

37   kyrs (*2*) and can be resolved into two distinct marine extinction pulses, with the respective kill

38   mechanisms appearing to be ecologically selective (*3*). The first occurred in the latest Permian

39   (Extinction Pulse 1; EP1) and was followed by an interval of temporary recovery before the

40   second pulse (EP2) which occurred in the earliest Triassic. The direct cause of the mass

41   extinction is widely debated with a diverse range of overlapping mechanisms proposed,

42   including widespread water column anoxia (*4*), euxinia (*5*), global warming (*6*) and ocean

43   acidification (*7*).

44   Models of PTB ocean acidification suggest that a massive, and rapid, release of CO_2 from

45   Siberian Trap volcanism, acidified the ocean (*7*). Indirect evidence for acidification comes from

46   the interpretation of faunal turnover records (*3, 8*), potential dissolution surfaces (*9*) and Ca

47   isotope data (*7*). A rapid input of carbon is also potentially recorded in the negative carbon

48   isotope excursion (CIE) that characterizes the PTB (*10, 11*) . The interpretation of these records

49   is, however, debated (*12*), and of great importance to understanding the current threat of

50   anthropogenically-driven ocean acidification (*11*).

51   Here, we test the ocean acidification hypothesis by presenting a novel proxy record of

52   ocean pH across the PTB, using the boron isotope composition of marine carbonates ($\delta^{11}B_{carb}$)

53   (SM sections 2 to 4). We then employ a carbon cycle model (SM sections 3 to 5) to explore

54   ocean carbonate chemistry and pH scenarios that are consistent with our $\delta^{11}B$ data and published

55   records of carbon cycle disturbance and environmental conditions. The quantitative model uses

56   previous estimates for background Early Permian conditions (*13*) suggesting either high pCO$_2$

57   (CO$_2$*Hi:* ~10 PAL, pH ~7.5 $\delta^{11}B_{SW}$ ~36.8‰), or low pCO$_2$ (CO$_2$*Lo:* ~3 PAL, pH ~8, $\delta^{11}B_{SW}$

58   ~34‰) (see SM sections 5 and 6 for further details). Through this combined geochemical,

59   geological and modelling approach we are able to produce an envelope that encompasses the

60   most realistic range in pH, which then allows us to resolve three distinct chronological phases of

61   carbon cycle perturbation, each with very different environmental consequences for the Late
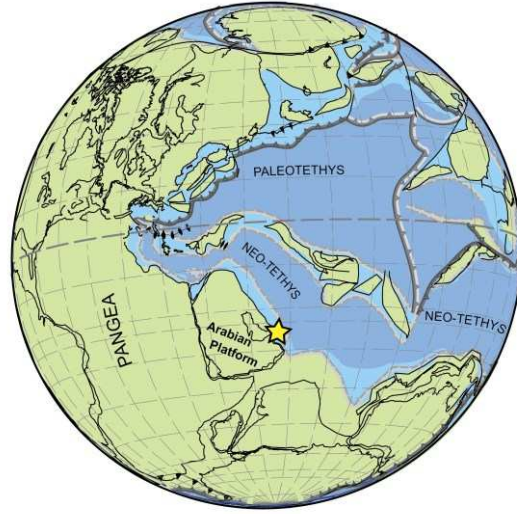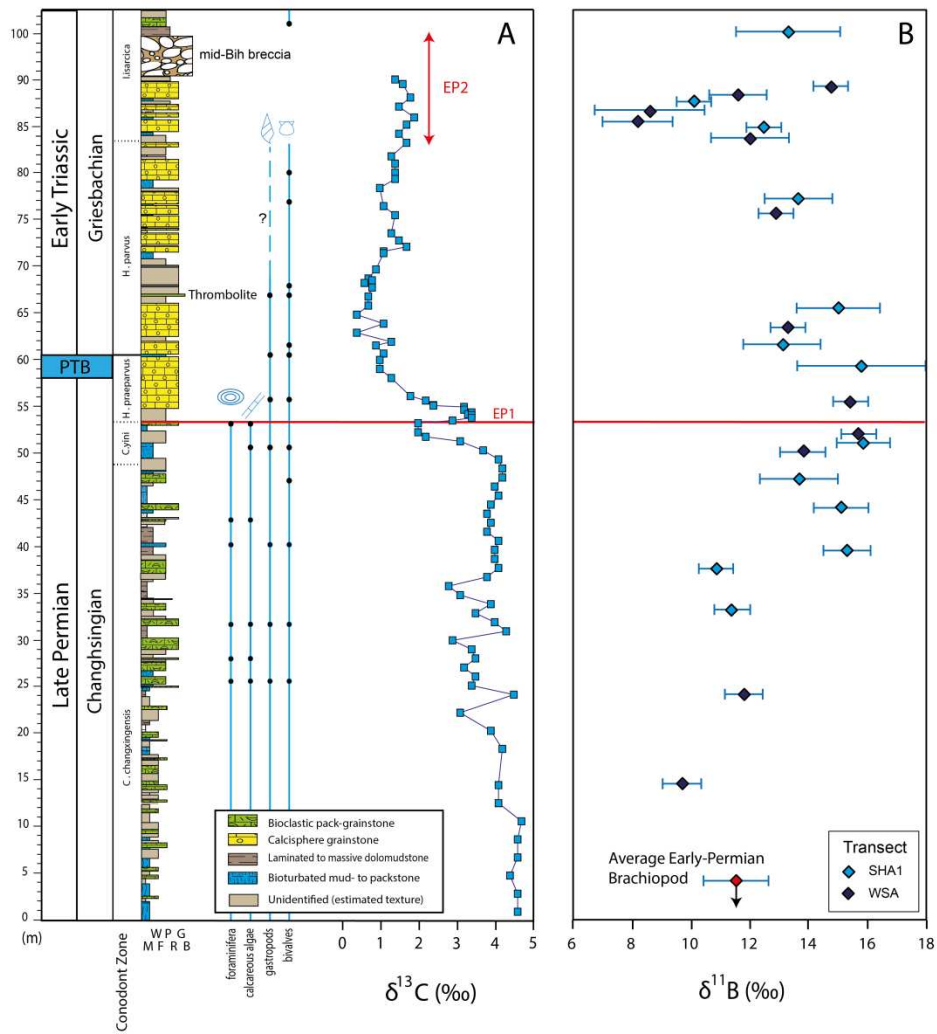
62   Permian-Early Triassic Earth system.

Figure 1

Figure 2

65   We analyzed boron isotope data from two complementary transects in a shallow marine,

66   open water carbonate succession from the United Arab Emirates (U.A.E.), where depositional

67   facies and $\delta^{13}C_{carb}$ are well constrained (*14*) (see SM sections 1 and 2). During the Permian-

68   Triassic the U.A.E formed an expansive carbonate platform that remained connected to the

69   central Neo-Tethyan Ocean (*15*) (Fig 1). The run-up to PTB in the Tethys is characterized by

70   two negative $\delta^{13}C$ excursions interrupted by a short-term positive event (*10*). There is no

71   consensus as to the cause of this rebound event and so we focus on the broader $\delta^{13}C$ trend. Our

72      $\delta^{13}C$ transect (Fig. 2) starts in the Changhsingian with a gradual decreasing trend, interrupted by

73   the first negative shift in $\delta^{13}C$ at EP1 (at 53 m or ~251.96 Ma, Fig. 2). This is followed by the

74   minor positive 'rebound' event (at 54 m or ~251.95 Ma, Fig. 2) prior to the minima of the second

75   phase of the negative CIE (58-60 m or ~251.92 Ma, Figs. 2 and 3) that marks the PTB itself.

76   After the CIE minimum, $\delta^{13}C$ gradually increases to ~1.8‰ and remains relatively stable during

77   earliest Triassic and across EP2.

78   Our boron isotope transect shows a quite different pattern. $\delta^{11}B$ is persistently low (Fig. 2),

79   at the start of our record during the late-Changhsingian (Late Permian), with an average of 10.9 ±

80   0.9‰ (1σ). This is in agreement with $\delta^{11}B$ values (average of 10.6 ± 0.6‰, 1σ) reported for

81   early-Permian brachiopods (*16*). Further up section (at ~40 m or ~252.04 Ma, Fig. 2), there is a

82   stepped increase in $\delta^{11}B$ to 15.3‰, and by implication an increase in ocean pH of ~0.4-0.5 pH

83   units (Fig. 3). Then $\delta^{11}B$ values remain relatively stable, scattering around 14.8‰ (± 1.0, 1σ) and

84   implying variations within 0.1-0.2 pH units, into the Early Griesbachian (Early Triassic) and

85   hence across EP1 and the period of carbon cycle disturbance (Figs. 2 and 3).

86   After $\delta^{13}C$ had increased and stabilized (at ~85 m or ~251.88 Ma, Fig. 2), $\delta^{11}B$ begins to

87   decrease rapidly to 8.2‰, implying a sharp drop in pH of ~0.6-0.7 pH units. The $\delta^{11}B$ minimum

Figure 3
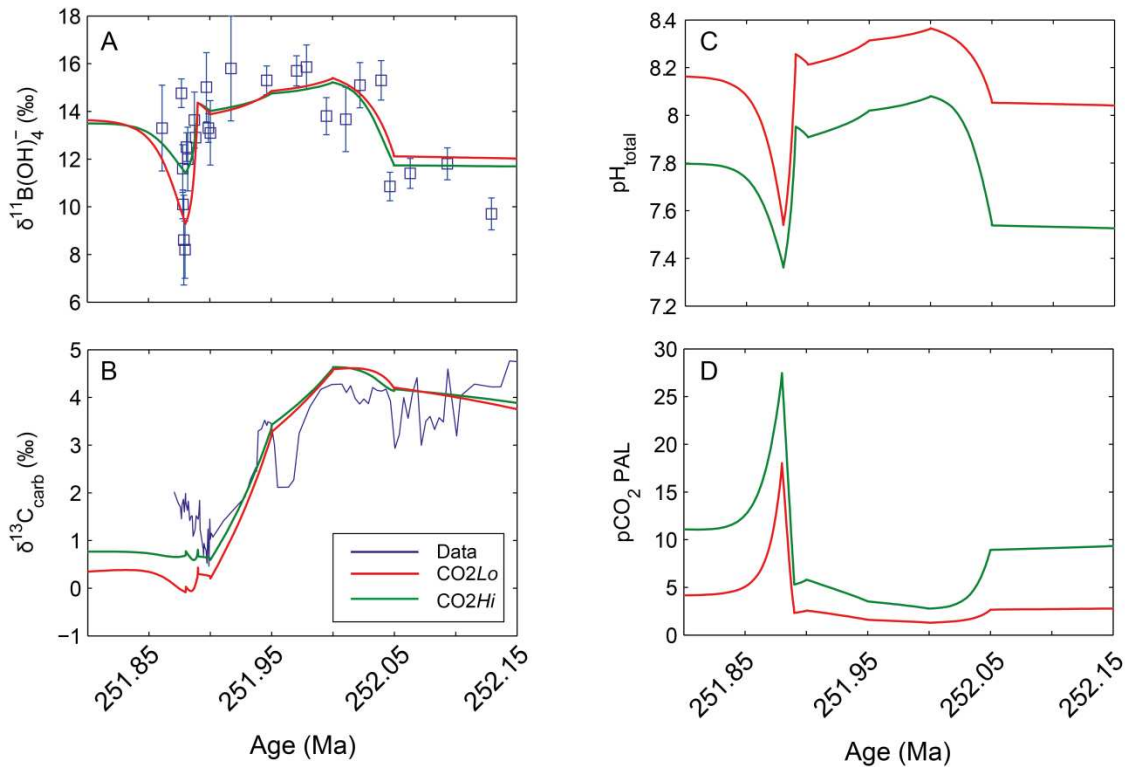
is coincident with the interval identified as EP2. This ocean acidification event is short-lived

(~10 kyrs) and $\delta^{11}B$ values quickly recover toward the more alkaline values evident during EP1

(average of ~14‰).

The initial rise in ocean pH of ~0.4-0.5 units during the Late Permian (Fig. 3) suggests

a large increase in carbonate alkalinity (17). We are able to simulate the observed rise in $\delta^{11}B$

and pH through different model combinations of increasing silicate weathering, increased pyrite

deposition (18), an increase in carbonate weathering and a decrease in shallow marine carbonate

depositional area (see SM section 6.1). Both silicate weathering and pyrite deposition result in a

large drop in pCO$_2$ (and temperature) for a given increase in pH and saturation state (Ω). There is

no evidence for a large drop in pCO$_2$, and independent proxy data indicate only a minor

temperature decrease of a few degrees C during the Changsingian (19), suggesting that these

mechanisms alone cannot explain the pH increase (see sensitivity tests in SM section 6.1).

6

100   Conversely, an increase in carbonate input or a reduction in rates of carbonate deposition both

101   result in increases in Ω, with a greater impact on pH per unit decrease in pCO$_2$ and temperature

102   (see Fig. S6).

103   This suggested decrease in carbonate sedimentation is consistent with the decrease in

104   depositional shelf area that occurred due to the 2nd order regression of the Late Permian ([20]).

105   With the added expansion of anoxia into shelf environments ([21]) this would effectively create

106   both bottom-up and top-down pressures to reduce the area of potential carbonate sedimentation.

107   Sea level fall also exposed carbonates to weathering ([20]), which would have further augmented

108   the alkalinity influx. The pH increase event supports the CO$_2$*Lo* initialisation scenario (CO$_2$ ~3

109   PAL, pH ~8, δ^{11}B$_{SW}$ ~34‰) as the simulated CO$_2$ and temperature decrease is much reduced,

110   and therefore more consistent with independent proxy data ([22]), compared to CO$_2$*Hi* (CO$_2$ ~10

111   PAL, pH ~7.5 δ^{11}B$_{SW}$ ~36.8‰) (Fig. 3D).

112   Prior to EP1, δ^{13}C$_{carb}$ values begin to decrease before reaching the minimum of the

113   globally recognized negative CIE at the PTB (Fig. 2). At this time both δ^{11}B and ocean pH

114   remained stable. Hypotheses to explain the negative CIE require the input of isotopically light

115   carbon, such as from volcanism ([14, 23]) with the assimilation of very light organic carbon from

116   the surrounding host rock ([24]), methane destabilization ([22]), collapse of the biological pump

117   ([15]), and/or a decrease in the burial of terrestrial carbon ([16]). We can simulate the observed drop

118   in δ^{13}C$_{carb}$, whilst remaining within the uncertainty of the δ^{11}B data (Fig. 3), by combining a

119   cessation of terrestrial carbon burial with a relatively slow (50 kyr) carbon injection from any of

120   the above sources (see section S6.2.4, Fig S8). A small source of methane (3.2 x10^{17} mol C with

121   δ^{13}C = -50‰) gives the least change in δ^{11}B and pH, whilst either a larger source of organic

122 carbon ($\sim6.5\times10^{17}$ mol C with $\delta^{13}C$ = -25‰) or a mixture of mantle and lighter carbon sources

123 ($\sim1.3\times10^{18}$ mol C with $\delta^{13}C$ = -12.5‰) are still within the measured uncertainty in $\delta^{11}B$.

124 This relatively slow carbon addition minimises the tendency for a transient decline in

125 surface ocean pH in an ocean that was already primed with a high Ω and hence high buffering

126 capacity from the Late Permian. The global presence of microbial and abiotic carbonate fabrics

127 after EP1 (Fig. 2) (25) are indicative that this high Ω was maintained across the CIE. The carbon

128 injection triggers an increase in $p\text{CO}_2$, temperature and silicate weathering, thereby creating an

129 additional counterbalancing alkalinity flux. This is consistent with independent proxy data (6).

130 The alkalinity source may have been further increased through soil loss (26), the emplacement of

131 easily-weathered Siberian Trap basalt, or the impact of acid rain (27) that would have increased

132 weathering efficiency.

133 The negative $\delta^{11}B_{carb}$ excursion at 251.88 Ma represents a calculated pH decrease of up to

134 0.7 pH units. It coincides with the second pulse of the extinction (Fig. 2), which preferentially

135 affected the heavily calcifying, physiologically un-buffered and sessile organisms (3). This was

136 also accompanied by the temporary loss of abiotic and microbial carbonates throughout the

137 Tethys (28, 29) thereby suggesting a coeval decrease in Ω (30). To overwhelm the buffering

138 capacity of the ocean and decrease pH in this way requires a second, more abrupt injection of

139 carbon to the atmosphere, yet remarkably, the acidification event occurs after the decline in $\delta^{13}C$,

140 when $\delta^{13}C$ has rebounded somewhat and is essentially stable (Fig. 2).

141 Unlike the first carbon injection, the lack of change in $\delta^{13}C$ at this time rules out very

142 ^{13}C-depleted carbon sources, because no counterbalancing strongly ^{13}C-enriched source exists.

143 Instead, it requires a carbon source near $\sim0‰$. A plausible scenario for this is the decarbonation

144 of overlying carbonate host rock, into which the Siberian Traps intruded (24) or the direct

145 assimilation of carbonates and evaporites into the melt (*31*). Host carbonates would have had

146 $\delta^{13}C$ ~+2-4‰, which when mixed with mantle carbon (~-5‰), potentially produces a source

147 near 0‰. We can simulate the sharp drop in pH and stable $\delta^{13}C$ values (Fig. 3) through a large

148 and rapid carbon release of 2×10^{18} mol C over 10 kyr (Fig S8). This second rapid carbon release

149 produces a sharp rise in pCO_2 to ~20 PAL and warming of ~15˚C, consistent with the

150 observation of peak temperatures after EP1 (*26*). Initialization of the carbon cycle model under

151 CO_2Hi cannot generate the magnitude of $\delta^{11}B$ drop (Fig. 3A) because the non-linear relation

152 between pH and $\delta^{11}B$ fractionation sets a lower limit of $\delta^{11}B$ at ~10‰ in this case (Fig. S3). Thus

153 low initial CO_2 of ~3 PAL in the late Permian (CO_2Lo) is more consistent with the data

154 presented here.

155   The documented acidification event lasted for only ~10 kyrs. This time span is consistent

156 with the modelled timescale required to replenish the ocean with alkalinity, as carbonate

157 deposition is reduced and weathering is increased under higher pCO_2 and global temperatures.

158 Increased silicate weathering rates drive further CO_2 drawdown resulting in stabilization (Fig.

159 S7). High global temperature (*6*) and increased silicate weathering are consistent with a sudden

160 increase in both $^{87}Sr/^{86}Sr$ (*32*) and sedimentation rates (*26*) in the Griesbachian.

161   The Permo-Triassic transition was a time of extreme environmental change, and our

162 combined data and modeling approach falsifies several mechanisms for the changes observed.

163 Whilst the coincident stresses of anoxia, increasing temperatures, and ecosystem restructuring

164 were important during this interval, the $\delta^{11}B$ excursion strongly suggests that widespread ocean

165 acidification was the driver of the second pulse of the mass extinction, and thus ultimately ended

166 the temporary recovery (*3*) from the first extinction pulse. The carbon release required to drive

167 the observed acidification event occurred at a rate comparable to the current anthropogenic

168   perturbation, but far exceeded it in expected magnitude (*33*). We show that such a rapid rate is

169   critical to causing the combined synchronous decrease in both pH and saturation state that

170   defines an ocean acidification event (*11*).

171

172

References and Notes

1. D. H. Erwin, The Permo-Triassic Extinction. *Nature* **367**, 231-236 (1994).

2. S. D. Burgess, S. A. Bowring, S. Z. Shen, High-precision timeline for Earth's most severe extinction. *Proceedings of the National Academy of Sciences of the United States of America* **111**, 3203-3204 (2014).

3. H. J. Song, P. B. Wignall, J. A. Tong, Y. Hongfu, Two pulses of extinction during the Permian-Triassic crisis. *Nat. Geosci.* **6**, 52-56 (2012).

4. P. B. Wignall, R. J. Twitchett, Oceanic anoxia and the end Permian mass extinction. *Science* **272**, 1155-1158 (1996).

5. K. Grice, C. Q. Cao, G. D. Love, M. E. Bottcher, R. J. Twitchett, E. Grosjean, R. E. Summons, S. C. Turgeon, W. Dunning, Y. G. Jin, Photic zone euxinia during the Permian-Triassic superanoxic event. *Science* **307**, 706-709 (2005); (10.1126/science.1104323).

6. Y. D. Sun, M. M. Joachimski, P. B. Wignall, C. B. Yan, Y. L. Chen, H. S. Jiang, L. N. Wang, X. L. Lai, Lethally Hot Temperatures During the Early Triassic Greenhouse. *Science* **338**, 366-370 (2012); (10.1126/science.1224126).

7. J. L. Payne, A. V. Turchyn, A. Paytan, D. J. DePaolo, D. J. Lehrmann, M. Y. Yu, J. Y. Wei, Calcium isotope constraints on the end-Permian mass extinction. *Proceedings of the National Academy of Sciences of the United States of America* **107**, 8543-8548 (2010); (10.1073/pnas.0914065107).

8. A. H. Knoll, R. K. Barnbach, J. L. Payne, S. Pruss, W. W. Fischer, Paleophysiology and end-Permian mass extinction. *Earth and Planetary Science Letters* **256**, 295-313 (2007); (10.1016/j.epsl.2007.02.018).

9. J. L. Payne, D. J. Lehrmann, D. Follett, M. Seibel, L. R. Kump, A. Riccardi, D. Altiner, H. Sano, J. Wei, Erosional truncation of uppermost Permian shallow-marine carbonates and implications for Permian-Triassic boundary events. *Geol. Soc. Am. Bull.* **119**, 771-784 (2007); (10.1130/b26091.1).

10. C. Korte, H. W. Kozur, Carbon-isotope stratigraphy across the Permian-Triassic boundary: A review. *Journal of Asian Earth Sciences* **39**, 215-235 (2010); (10.1016/j.jseaes.2010.01.005).

11. B. Hönisch, A. Ridgwell, D. N. Schmidt, E. Thomas, S. J. Gibbs, A. Sluijs, R. Zeebe, L. Kump, R. C. Martindale, S. E. Greene, W. Kiessling, J. Ries, J. C. Zachos, D. L. Royer, S. Barker, T. M. Marchitto, Jr., R. Moyer, C. Pelejero, P. Ziveri, G. L. Foster, B. Williams, The Geological Record of Ocean Acidification. *Science* **335**, 1058-1063 (2012); (10.1126/science.1208277).

12. C. L. Blätter, H. C. Jenkyns, L. M. Reynard, G. M. Henderson, Signifcant increases in global weathering during Oceanic Anoxic Events 1a and 2 indicated by calcium isotopes. *Earth and Planetary Science Letters* **309**, 77-88 (2011).

208　13.　Y. Cui, L. R. Kump, Global warming and the end-Permian extinction event: Proxy and
209　　　modeling perspectives. *Earth-Science Reviews*, (2014);
210　　　(http://dx.doi.org/10.1016/j.earscirev.2014.04.007).

211　14.　M. O. Clarkson, S. Richoz, R. A. Wood, F. Maurer, L. Krystyn, D. J. McGurty, D. Astratti, A new
212　　　high-resolution delta C-13 record for the Early Triassic: Insights from the Arabian Platform.
213　　　*Gondwana Research* **24**, 233-242 (2013); (10.1016/j.gr.2012.10.002).

214　15.　G. M. Stampfli, G. D. Borel, A plate tectonic model for the Paleozoic and Mesozoic
215　　　constrained by dynamic plate boundaries and restored synthetic oceanic isochrons. *Earth*
216　　　*and Planetary Science Letters* **196**, 17-33 (2002); (Pii s0012-821x(01)00588-
217　　　x10.1016/s0012-821x(01)00588-x).

218　16.　M. M. Joachimski, L. Simon, R. van Geldern, C. Lecuyer, Boron isotope geochemistry of
219　　　Paleozoic brachiopod calcite: Implications for a secular change in the boron isotope
220　　　geochemistry of seawater over the Phanerozoic. *Geochimica et Cosmochimica Acta* **69**, 4035-
221　　　4044 (2005); (10.1016/j.gca.2004.11.017).

222　17.　the alternative way to drive an increase in pH would be through a removal of carbon,
223　　　however this would be evident in the $\delta^{13}C$ record so we can rule it out.

224　18.　Bacterial Sulfate Reduction (BSR) is a net source of alkalinity if the generated H_2S is buried
225　　　as pyrite. Pyrite deposition is seen widely in certain setting during the Late Permian to PTB.
226　　　See SI for further information.

227　19.　M. M. Joachimski, X. L. Lai, S. Z. Shen, H. S. Jiang, G. M. Luo, B. Chen, J. Chen, Y. D. Sun, Climate
228　　　warming in the latest Permian and the Permian-Triassic mass extinction. *Geology* **40**, 195-
229　　　198 (2012); (Doi 10.1130/G32707.1).

230　20.　H. Yin, H. Jiang, W. Xia, Q. Feng, N. Zhang, J. Shen, The end-Permian regression in South China
231　　　and its implication on mass extinction. *Earth-Sci. Rev.* **137**, 19-33 (2014);
232　　　(http://dx.doi.org/10.1016/j.earscirev.2013.06.003).

233　21.　P. B. Wignall, R. J. Twitchett, Extent, duration, and nature of the Permian-Triassic
234　　　superanoxic event. *Catastrophic Events and Mass Extinctions: Impacts and Beyond*, 395-413
235　　　(2002).

236　22.　E. S. Krull, G. J. Retallack, $\delta^{13}C$ depth profiles from paleosols across the Permian-Triassic
237　　　boundary: Evidence for methane release. *Geol. Soc. Am. Bull.* **112**, 1459-1472 (2000);
238　　　(10.1130/0016-7606(2000)112%3c;1459:cdpfpa%3e;2.0.co;2).

239　23.　C. Korte, P. Pande, P. Kalia, H. W. Kozur, M. M. Joachimski, H. Oberhaensli, Massive volcanism
240　　　at the Permian-Triassic boundary and its impact on the isotopic composition of the ocean
241　　　and atmosphere. *Journal of Asian Earth Sciences* **37**, 293-311 (2010);
242　　　(10.1016/j.jseaes.2009.08.012).

243　24.　H. Svensen, S. Planke, A. G. Polozov, N. Schmidbauer, F. Corfu, Y. Y. Podladchikov, B. Jamtveit,
244　　　Siberian gas venting and the end-Permian environmental crisis. *Earth and Planetary Science*
245　　　*Letters* **277**, 490-500 (2009); (10.1016/j.epsl.2008.11.015).

246 25. A. D. Woods, Assessing Early Triassic Paleoceanographic conditions vias unusual
247   sedimentary fabrics and features. *Earth-Sci. Rev.*, (2013);
248   (http://dx.doi.org/10.1016/j.earscirev.2013.08.015).

249 26. T. J. Algeo, Z. Q. Chen, M. L. Fraiser, R. J. Twitchett, Terrestrial-marine teleconnections in the
250   collapse and rebuilding of Early Triassic marine ecosystems. *Paleogeography*
251   *Paleoclimatology Paleoecology* **308**, 1-11 (2011); (10.1016/j.paleo.2011.01.011).

252 27. B. A. Black, J. F. Lamarque, C. A. Shields, L. T. Elkins-Tanton, J. T. Kiehl, Acid rain and ozone
253   depletion from pulsed Siberian Traps magmatism. *Geology* **42**, 67-70 (2014); (Doi
254   10.1130/G34875.1).

255 28. A. Baud, S. Richoz, S. Pruss, The lower Triassic anachronistic carbonate facies in space and
256   time. *Global and Planetary Change* **55**, 81-89 (2007); (10.1016/j.gloplacha.2006.06.008).

257 29. S. Richoz, L. Krystyn, A. Baud, R. Brandner, M. Horacek, P. Mohtat-Aghai, Permian-Triassic
258   boundary interval in the Middle East (Iran and N. Oman): Progressive environmental
259   change from detailed carbonate carbon isotope marine curve and sedimentary evolution.
260   *Journal of Asian Earth Sciences* **39**, 236-253 (2010); (10.1016/j.jseaes.2009.12.014).

261 30. Note that the system connot be undersaturated as this precludes the preservation of the
262   boron isotope record.

263 31. B. A. Black, L. T. Elkins-Tanton, M. C. Rowe, I. U. Peate, Magnitude and consequences of
264   volatile release from the Siberian Traps. *Earth and Planetary Science Letters* **317**, 363-373
265   (2012); (Doi 10.1016/J.Epsl.2011.12.001).

266 32. C. Korte, H. W. Kozur, M. M. Joachimski, H. Strauss, J. Veizer, L. Schwark, Carbon, sulfur,
267   oxygen and strontium isotope records, organic geochemistry and biostratigraphy across the
268   Permian/Triassic boundary in Abadeh, Iran. *International Journal of Earth Sciences* **93**, 565-
269   581 (2004); (Doi 10.1007/S00531-004-0406-7).

270 33. The imposed perturbation for the acidification event is 24000 PgC compared to the
271   estimates of 4-5000PgC that could be generated from conventional fossil fuels. Upper
272   estimates using unconvential fossil fuels (e.g. methane hydrates) can reach ~ 24000 PgC

273 34. F. Maurer, R. Martini, R. Rettori, H. Hillgartner, S. Cirilli, The geology of Khuff outcrop
274   analogues in the Musandam Peninsula, United Arab Emirates and Oman. *GeoArabia* **14**, 125-
275   158 (2009).

276 35. S. Z. Shen, C. Q. Cao, H. Zhang, S. A. Bowring, C. M. Henderson, J. L. Payne, V. I. Davydov, B.
277   Chen, D. X. Yuan, Y. C. Zhang, W. Wang, Q. F. Zheng, High-resolution delta C-13(carb)
278   chemostratigraphy from latest Guadalupian through earliest Triassic in South China and
279   Iran. *Earth and Planetary Science Letters* **375**, 156-165 (2013); (Doi
280   10.1016/J.Epsl.2013.05.020).

281 36. B. Koehrer, M. Zeller, T. Aigner, M. Poeppelreiter, P. Milroy, H. Forke, S. Al-Kindi, Facies and
282   stratigraphic framework of a Khuff outcrop equivalent: Saiq and Mahil formations, Al Jabal
283   al-Akhdar, Sultanate of Oman. *GeoArabia* **15**, 91-156 (2010).

284 37. S. Kasemann, A. Meixner, A. Rocholl, T. Vennemann, M. Rosner, A. K. Schmitt, M.
285 Wiedenbeck, Boron and oxygen isotope composition of certified reference materials NIST
286 SRM 610/612 and reference materials JB-2 and JR-2. *Geostandards Newsletter-the Journal of*
287 *Geostandards and Geoanalysis* **25**, 405-416 (2001); (Doi 10.1111/J.1751-
288 908x.2001.Tb00615.X).

289 38. J. Vogl, M. Rosner, W. Pritzkow, Development and validation of a single collector SF-ICPMS
290 procedure for the determination of boron isotope ratios in water and food samples. *Journal*
291 *of Analytical Atomic Spectrometry*, **26**, 861-869 (2011).

292 39. S. A. Kasemann, SD. N. Schmidt, J. Bijma, J., G. L. Foster, In situ boron isotope analysis in
293 marine carbonates and its application for foraminifera and paleo-pH. *Chemical Geology*,.
294 **260,** 138-147 (2009)

295 40. S. A. Kasemann, C. J. Hawkesworth, A. R. Prave, A. E. Fallick, P. N. Pearson, Boron and calcium
296 isotope composition in Neoproterozoic carbonate rocks from Namibia: evidence for
297 extreme environmental change. *Earth and Planetary Science Letters* **231**, 73-86 (2005); (Doi
298 10.1016/J.Epsl.2004.12.006).

299 41. F. Ohnemüller, A. R. Prave, A. E. Fallick, S. A. Kasemann, Ocean acidification in the aftermath
300 of the Marinoan glaciation. *Geology,* doi:10.1130/G35937.1 (2014).

301 42. P. B. Wignall, A. Hallam, Facies change and the end-Permian mass extinction in SE Sichuan,
302 China. *Palaios* **11**, 587-596 (1996).

303 43. L. Breesch, R. Swennen, B. Dewever, F. Roure, B. Vincent, Diagenesis and fluid system
304 evolution in the northern Oman Mountains, United Arab Emirates: Implications for
305 petroleum exploration. *GeoArabia* **16**, 111-148 (2011).

306 44. S. B. Jacobsen, A. J. Kaufman, The Sr, C and O isotopic evolution of Neoproterozoic seawater.
307 *Chem. Geol.* **161**, 37-57 (1999); (Doi 10.1016/S0009-2541(99)00080-7).

308 45. S. A. Kasemann, A. R. Prave, A. E. Fallick, C. J. Hawkesworth, K. H. Hoffmann, Neoproterozoic
309 ice ages, boron isotopes, and ocean acidification: Implications for a snowball Earth. *Geology*
310 **38**, 775-778 (2010); (10.1130/g30851.1).

311 46. G. Paris, A. Bartolini, Y. Donnadieu, V. Beaumont, J. Gaillardet, Investigating boron isotopes
312 in a middle Jurassic micritic sequence: Primary vs. diagenetic signal. *Chem. Geol.* **275**, 117-
313 126 (2010); (10.1016/j.chemgeo.2010.03.013).

314 47. A. J. Spivack, J. M. Edmond, Boron Isotope Exchange between Seawater and the Oceanic-
315 Crust. *Geochimica et Cosmochimica Acta* **51**, 1033-1043 (1987); (Doi 10.1016/0016-
316 7037(87)90198-0).

317 48. J. Veizer, D. Ala, K. Azmy, P. Bruckschen, D. Buhl, F. Bruhn, G.A. F. Carden, A. Diener, S.
318 Ebneth, Y. Godderis, T. Jasper, C. Korte, F. Pawellek, O. Podlaha, and Strauss, H. "[87]Sr/[86]Sr,
319 δ^{13}C and δ^{18}O evolution of Phanerozoic seawater". *Chemical Geology* **161**: 59-88 (1999).

320 49. D. Lemarchand, J. Gaillardet, E. Lewin, C. J. Allegre, The influence of rivers on marine boron
321 isotopes and implications for reconstructing past ocean pH. *Nature* **408**, 951-954 (2000).

322   50.   A. G. Dickson, Thermodynamics of the dissociation of boric-acid in synthetic seawater from
323   273.15-k to 318.15-k. *Deep-Sea Research Part a-Oceanographic Research Papers* **37**, 755-766
324   (1990).

325   51.   M. Schobben, M. M. Joachimski, D. Korn, L. Leda, C. Korte, Paleotethys seawater temperature
326   rise and an intensified hydrological cycle following the end-Permian mass extinction.
327   *Gondwana Research*, (2013); (http://dx.doi.org/10.1016/j.gr.2013.07.019).

328   52.   J. T. Kiehl, C. A. Shields, Climate simulation of the latest Permian: Implications for mass
329   extinction. *Geology* **33**, 757-760 (2005); (Doi 10.1130/G21654.1).

330   53.   R. A. Locarnini, A. V. Mishonov, J. I. Antonov, T. P. Boyer, H. E. Garcia, in *NOAA Atlas NESDIS*
331   *61*, S. Levitus, Ed. (U.S. Government Printing Office, Washington, D.C, 2006), vol. 1:
332   Temperature.

333   54.   P. N. Pearson, M. R. Palmer, Atmospheric carbon dioxide concentrations over the past 60
334   million years. *Nature* **406**, 695-699 (2000).

335   55.   G. L. Foster, Seawater pH, PCO2 and [CO32-] variations in the Caribbean Sea over the last
336   130 kyr: A boron isotope and B/Ca study of planktic forminifera. *Earth and Planetary*
337   *Science Letters* **271**, 254-266 (2008); (10.1016/j.epsl.2008.04.015).

338   56.   B. Hönisch, N. G. Hemming, D. Archer, M. Siddall, J. F. McManus, Atmospheric Carbon Dioxide
339   Concentration Across the Mid-Pleistocene Transition. *Science* **324**, 1551-1554 (2009); (Doi
340   10.1126/Science.1171477).

341   57.   N. G. Hemming, G. N. Hanson, Boron isotopic composition and concentration in modern
342   marine carbonates. *Geochimica et Cosmochimica Acta* **56**, 537-543 (1992).

343   58.   N. G. Hemming, B. Honisch, A critical review and recent advances in the boron isotope
344   paleo-pH proxy. *Geochimica et Cosmochimica Acta* **69**, A129-A129 (2005).

345   59.   K. Klochko, A. J. Kaufman, W. S. Yao, R. H. Byrne, J. A. Tossell, Experimental measurement of
346   boron isotope fractionation in seawater. *Earth and Planetary Science Letters* **248**, 276-285
347   (2006); (10.1016/j.epsl.2006.05.034).

348   60.   E. Lewis, D. W. R. Wallace. (Oak Ridge, 1998).

349   61.   J. W. B. Rae, G. L. Foster, D. N. Schmidt, T. Elliott, Boron isotopes and B/Ca in benthic
350   foraminifera: Proxies for the deep ocean carbonate system. *Earth and Planetary Science*
351   *Letters* **302**, 403-413 (2011).

352   62.   M. Pagani, J. C. Zachos, K.H. Freeman, B. Tipple, H. Bohaty, Marked decline in atmospheric
353   carbon dioxide concentrations during the Paleogene. *Science* **309**, 600-603 (2005)

354   63.   A. Sanyal, M. Nugent, R. J. Reeder, J. Buma, Seawater pH control on the boron isotopic
355   composition of calcite: Evidence from inorganic calcite precipitation experiments.
356   *Geochimica et Cosmochimica Acta* **64**, 1551-1555 (2000).

357   64.   K. Klochko, G. D. Cody, J. A. Tossell, P. Dera, A. J. Kaufman, Re-evaluating boron speciation in
358   biogenic calcite and aragonite using B-11 MAS NMR. *Geochimica et Cosmochimica Acta* **73**,
359   1890-1900 (2009); (10.1016/j.gca.2009.01.002).

360   65.   R. A. Berner, Examination of hypotheses for the Permo-Triassic boundary extinction by
361   carbon cycle modeling. *Proceedings of the National Academy of Sciences of the United States*
362   *of America* **99**, 4172-4177 (2002); (10.1073/pnas.032095199).

363   66.   M. R. Rampino, K. Caldeira, Major perturbation of ocean chemistry and a 'Strangelove Ocean'
364   after the end-Permian mass extinction. *Terra Nova* **17**, 554-559 (2005); (10.1111/j.1365-
365   3121.2005.00648.x).

366   67.   J. Payne, L. Kump, Evidence for recurrent Early Triassic massive volcanism from
367   quantitative interpretation of carbon isotope fluctuations. *Earth and Planetary Science*
368   *Letters* **256**, 264-277 (2007); (10.1016/j.epsl.2007.01.034).

369   68.   K. Caldeira, J. F. Kasting, The life span of the biosphere revisited. *Nauture* **360**, 721-723
370   (1992).

371   69.   J. M. Bergman, T. M. Lenton, A. J. Watson, COPSE: A new model of biogeochemical cycling
372   over Phanerozoic time. *American Journal of Science* **304**, (2004).

373   70.   A. F. Hofmann, K. Soetaert, J. J. Middelburg, F. J. R. Meysman, AquaEnv : An Aquatic Acid–
374   Base Modelling Environment in R. *Aquatic Geochemistry* **16**, 507-546 (2010);
375   (10.1007/s10498-009-9084-1).

376   71.   R. E. Zeebe, P. Westbrooke, A simple model for the CaCO3 saturation state of the ocean: The
377   "Strangelove," the "Neritan," and the "Cretan" Ocean. *Geochemistry Geophysics Geosystems*
378   **4**, (2003).

379   72.   J. Zhang, P. D. Quay, D. O. Wilbur, Carbon isotope fractionation during gas-water exchange
380   and dissolution of CO2. *Geochimica et Cosmochimica Acta* **59**, 107-114 (1995).

381   73.   H. D. Holland, in *Treatise on Geochemistry: Vol 6 The oceans and marine geochemistry,* H. D.
382   Holland, K. K. Turekian, Eds. (Elsevier Academic Press, 2003), pp. 583-625.

383   74.   H. Song, J. Tong, T. J. Algeo, H. Song, H. Qiu, Y. Zhu, L. Tian, S. Bates, T. W. Lyons, G. Luo, L. R.
384   Kump, Early Triassic seawater sulfate drawdown. *Geochimica et Cosmochimica Acta* **128**,
385   95-113 (2014); (10.1016/j.gca.2013.12.009).

386   75.   G. Luo, L. R. Kump, Y. Wang, J. Tong, M. a. Arthur, H. Yang, J. Huang, H. Yin, S. Xie, Isotopic
387   evidence for an anomalously low oceanic sulfate concentration following end-Permian mass
388   extinction. *Earth and Planetary Science Letters* **300**, 101-111 (2010);
389   (10.1016/j.epsl.2010.09.041).

390   76.   S. Ben-Yaakov, M. B. Goldhaber, The influence of sea water composition on the apparent
391   constants of the carbonate system. *Deep Sea Research and Oceanographic Abstracts* **20**, 87-
392   99 (1973); (10.1016/0011-7471(73)90044-2).

393   77.   R. E. Zeebe, LOSCAR: Long-term Ocean-atmosphere-Sediment CArbon cycle Reservoir Model
394   v2.0.4. *Geoscientific Model Development* **5**, 149-166 (2012); (10.5194/gmd-5-149-2012).

395   78.   Y. Cui, L. R. Kump, Global warming and the end-Permian extinction event: Proxy and
396   modeling perspectives. (2014); (doi:10.1016/j.earscirev.2014.04.007).

397   79.   Y. Cui, L. R. Kump, A. Ridgwell, Initial assessment of the carbon emission rate and climatic
398   consequences during the end-Permian mass extinction. *Paleogeography Paleoclimatology*
399   *Paleoecology* **389**, 128-136 (2013).

400   80.   T. J. Algeo, K. Kuwahara, H. Sano, S. Bates, T. Lyons, E. Elswick, L. Hinnov, B. Ellwood, J.
401   Moser, J. B. Maynard, Spatial variation in sediment fluxes, redox conditions, and productivity
402   in the Permian–Triassic Panthalassic Ocean. *Paleogeography, Paleoclimatology, Paleoecology*
403   **308**, 65-83 (2011); (10.1016/j.paleo.2010.07.007).

404   81.   T. J. Algeo, R. J. Twitchett, Anomalous Early Triassic sediment fluxes due to elevated
405   weathering rates and their biological consequences. *Geology* **38**, 1023-1026 (2010);
406   (10.1130/g31203.1).

407   82.   G. A. Brennecka, A. D. Herrmann, T. J. Algeo, A. D. Anbar, Rapid expansion of oceanic anoxia
408   immediately before the end-Permian mass extinction. *Proceedings of the National Academy*
409   *of Sciences of the United States of America* **108**, 17631-17634 (2011);
410   (10.1073/pnas.1106039108).

411   83.   S. E. Grasby, B. Beauchamp, Latest Permian to Early Triassic basin-to-shelf anoxia in the
412   Sverdrup Basin, Arctic Canada. *Chem. Geol.* **264**, 232-246 (2009); (Doi
413   10.1016/J.Chemgeo.2009.03.009).

414   84.   C. Winguth, A. M. E. Winguth, Simulating Permian-Triassic oceanic anoxia distribution:
415   Implications for species extinction and recovery. *Geology* **40**, 127-130 (2012);
416   (10.1130/g32453.1).

417   85.   T. J. Algeo, C. M. Henderson, J. N. Tong, Q. L. Feng, H. F. Yin, R. V. Tyson, Plankton and
418   productivity during the Permian-Triassic boundary crisis: An analysis of organic carbon
419   fluxes. *Global and Planetary Change* **105**, 52-67 (2013); (Doi
420   10.1016/J.Gloplacha.2012.02.008).

421   86.   E. Tziperman, I. Halevy, D. T. Johnston, A. H. Knoll, D. P. Schrag, Biologically induced
422   initiation of Neoproterozoic snowball-Earth events. *Proceedings of the National Academy of*
423   *Sciences of the United States of America*, 1-6 (2011); (10.1073/pnas.1016361108).

424   87.   S. W. Poulton, D. E. Canfield, Ferruginous Conditions: A Dominant Feature of the Ocean
425   through Earth's History. *Elements* **7**, 107-112 (2011); (10.2113/gselements.7.2.107).

426   88.   H. Song, J. Tong, T. J. Algeo, H. Song, H. Qiu, Y. Zhu, L. Tian, S. Bates, T. W. Lyons, G. Luo, L. R.
427   Kump, Early Triassic seawater sulfate drawdown. *Geochimica et Cosmochimica Acta*,
428   (2013); (doi: http://dx.doi.org/10.1016/j.gca.2013.12.009).

429   89.   W. S. Broecker, S. Peacock, An ecologic explanation for the Permo-Triassic carbon and sulfur
430   isotope shifts. *Global Biogeochemical Cycles* **13**, 1167-1172 (1999).

431   90.   G. Luo, Y. Wang, K. Grice, S. Kershaw, T. J. Algeo, X. Ruan, H. Yang, C. Jia, S. Xie, Microbial–
432   algal community changes during the latest Permian ecological crisis: Evidence from lipid

433   biomarkers at Cili, South China. *Global and Planetary Change* **105**, 36-51 (2013);
434   (10.1016/j.gloplacha.2012.11.015).

435   91.   K. M. Meyer, M. Yu, A. B. Jost, B. M. Kelley, J. L. Payne, $\delta^{13}C$ evidence that high primary
436   productivity delayed recovery from end-Permian mass extinction. *Earth and Planetary*
437   *Science Letters* **302**, 378-384 (2011); (10.1016/j.epsl.2010.12.033).

438   92.   H. J. Song, J. N. Tong, Y. L. Xiong, D. Y. Sun, L. Tian, H. Y. Song, The large increase of
439        $\delta^{13}C(carb)$-depth gradient and the end-Permian mass extinction. *Sci. China-Earth Sci.* **55**,
440   1101-1109 (2012); (10.1007/s11430-012-4416-1).

441   93.   D. E. Ogden, N. H. Sleep, Explosive eruption of coal and basalt and the end-Permian mass
442   extinction. *Proceedings of the National Academy of Sciences of the United States of America*
443   **109**, 59-62 (2012); (10.1073/pnas.1118675109).

444   94.   M. K. Reichow, A. D. Saunders, R. V. White, M. S. Pringle, A. I. Al'Mukhamedov, A. I.
445   Medvedev, N. P. Kirda, Ar-40/Ar-39 dates from the West Siberian Basin: Siberian flood
446   basalt province doubled. *Science* **296**, 1846-1849 (2002).

447   95.   M. B. Harfoot, J. a. Pyle, D. J. Beerling, End-Permian ozone shield unaffected by oceanic
448   hydrogen sulphide and methane releases. *Nat. Geosci.* **1**, 247-252 (2008);
449   (10.1038/ngeo154).

450   96.   C. Ganino, N. T. Arndt, Climate changes caused by degassing of sediments during the
451   emplacement of large igneous provinces. *Geology* **37**, 323-326 (2009);
452   (10.1130/G25325A.1).

453

454

455

456

Fig. 1: Paleogeographic reconstruction for the Late Permian denoting the studied section Wadi Bih, in the Musandam Mountians of U.A.E that formed an extensive carbonate platform in the Neo-Tethyan Ocean. Modified from (*14*).

Fig. 2: Carbon cycle dynamics, macrofauna distribution (*34*), and Extinction Phase 1 (EP1) and Extinction Phase 2 interval (EP2) across the Permian Triassic Boundary for Wadi Bih, A: shallow water δ^{13}C record (*14*); B: Boron isotope (δ^{11}B) record (propagated uncertainty given as 2σf) and average Early Permian brachiopod value (n=5) (*16*). Blue symbols are for SHA1 transect, black symbols are for WSA transect. The two transects are separated by ~ 1km and facies are laterally continuous. Only *H. parvus* has been found so far in this section and the conodont zones with dashed line are identified from the δ^{13}C record (*34-36*).

Fig. 3: Model results of carbon cycle parameters for the two end-member CO_2 scenarios (CO_2Hi and CO_2Lo). A - Model reproduced δ^{11}B vs data. B – Modelled δ^{13}C vs data. C – Modelled pH

480   envelope incorporating uncertainty of $\delta^{11}B_{SW}$ and dynamic temperatures. D – calculated

481   atmospheric CO_2. See SM section 1.2 for details on age model.

482

483

489

490 # Supplementary Materials

491 **1. Materials and Methods**

492 **1.1 Sample Section**

493 Carbonate samples were obtained from a shallow-marine platform section at Wadi Bih on the

494 Musandam Peninsula, United Arab Emirates (UAE). GPS co-ordinate for main transect in Wadi

495 Shahha are N 025° 50′ 31.7″, E 056° 06′ 41.7″. This is a near-continuous and exclusively

496 shallow marine carbonate succession from the late Permian and entire Early Triassic that allows

497 analysis of a high-resolution signature in the absence of significant depth-dependent or

498 lithological controls (*14*). Late Permian facies are predominantly intertidal mud-and-wackestones

499 and open lagoon wackestones, occasional windward and leeward shoals of bioclastic pack-and-

500 grainstones (*34*). The PTB and Early Triassic are regionally represented by ooidal grainstones

501 and a thrombolite horizon (*14, 34*). Samples were taken from two transects Wadi Shahha (WSA)

502 and Sha (SHA1), ~1000 m apart.. Facies are laterally continuous and carbon isotopes were used

503 to ensure careful integration of the two datasets. For this study, we have analyzed 25 carbonate

504 samples in total, taken in approximately 1 to 10 m scale intervals and covering a total thickness

505 of 98 m, starting in the mid-Changhsingian (Permian), going up into the mid-Griesbachian

506 (Triassic) and bracketing the complete Permian Triassic Boundary (PTB) extinction event (Table

507 S1).

Table S1: Boron, carbon and oxygen isotope data from Wadi Bih; U.A.E.; pH values are derived from a simplified and non-dynamic calulation using the $\delta^{11}B_{SW}$ range given by the model calculation and a constant pK_B for 25°C, 35 psu, 0 dbar.

Sample	Height (m)	Lithology	Age (Ma)*	$\delta^{13}C$ (‰)	$\delta^{18}O$ (‰)	$\delta^{11}B$ (‰)[+]	$2\sigma f$ (‰)[#]	pH $\delta^{11}B_{SW}$ 34‰	pH $\delta^{11}B_{SW}$ 36.8‰
					Wadi Bih (25° 50' 31.2"N 56° 06' 41.7"E)				
WSA54	14.0	micritic mudstone	252.13	4.20	-2.40	9.7(3)	0.7	7.7	6.7
WSA49	24.0	micritic mudstone	252.09	4.60	-0.50	11.8(3)	0.7	8.0	7.6
SHA1 1	32.4	dolograinstone	252.06	4.23	-3.19	11.4(2)	0.6	7.9	7.5
SHA1 3	37.0	grainstone	252.05	4.22	-2.62	10.8(0)	0.6	7.9	7.4
SHA1 4	39.0	micritic mudstone	252.04	4.26	-2.51	15.3(6)	0.8	8.3	8.1
SHA1 7	43.8	bioclastic packstone	252.02	3.63	-2.65	15.1(7)	1.0	8.3	8.0
SHA1 8	47.0	bioclastic packstone	252.01			13.7(12)	1.4	8.2	7.9
WSA22a	50.0	micritic mudstone	252.00	3.80	-3.50	13.8(5)	0.8	8.2	7.9
SHA1 11	51.0	bioturbated mudston	251.98			15.9(7)	0.9	8.3	8.1
WSA21	52.0	micritic mudstone	251.97	2.10	-4.00	15.7(2)	0.6	8.3	8.1
WSA 17	55.0	micritic mudstone	251.95	2.54	-3.65	15.3(2)	0.6	8.3	8.1
SHA1 15	59.6	calcisphere grainston	251.92	0.52	-3.15	15.8(21)	2.2	8.3	8.1
SHA1 17	62.0	calcisphere grainston	251.90			13.1(12)	1.4	8.1	7.8
WSA12A	64.0	micritic mudstone	251.90	0.50	-3.40	13.3(0)	0.6	8.1	7.8
SHA1 20	66.0	calcisphere grainston	251.90			15.0(13)	1.5	8.3	8.0
WSA5A	77.0	micritic mudstone	251.89	1.50	-3.20	12.9(0)	0.6	8.1	7.8
SHA1 26	78.2	calcisphere grainston	251.89	1.21	-2.55	13.6(10)	1.2	8.2	7.9
WSA3	85.0	micritic mudstone	251.88	1.60	-2.60	12.0(12)	1.3	8.0	7.6
SHA1 30	86.2	calcisphere grainston	251.88			12.5(6)	0.6	8.1	7.7
WSA 2A	86.8	micritic mudstone	251.88	1.99	-2.96	8.2(10)	1.2	7.4	-
WSA2	88.0	micritic mudstone	251.88	1.60	-2.94	8.6(18)	1.9	7.5	< 7,0
WSA 1B	89.0	micritic mudstone	251.88	1.87	-3.26	10.1(2)	0.6	7.8	7.0
SHA1 32	90.2	calcisphere grainston	251.88	1.39	-3.40	11.6(8)	1.0	8.0	7.6
WSA1	91.0	micritic mudstone	251.88	1.46	-3.74	14.8(0)	0.6	8.2	8.0
SHA1 36	102.0	bioclastic packstone	251.86	1.79	-2.00	13.3(17)	1.8	8.1	7.8

* Ages are calculated based on tie points from Burgess et al.(2), see section S1.2
[+] external uncertainty for B isotope data are valid for the last digits (2σ)
[#] propagated uncerteinties for B isotope data

508

509

1.2 Age Model

510

511 The age model for this study was based on the most recent findings of Burgess et al., (*2*) (see

512 Table S1). The age tie points are 252.10 Ma for 20 m (Fig. 2) thought to be equivalent to Bed 22

513 in Meishan from the $\delta^{13}C$ record; 252.00 Ma for the decline in $\delta^{13}C$ at 49 m and 251.90 Ma for

514 the first occurrence of *H. parvus* at 61m. EP2 is known to occur at the end of the *I. staeschi* zone,

515 Bed 28 Meishan (*3*), which is not recorded in the Neo-Tethys but is equivalent to the carbon

516   isotope rise between the *H. Parvus* and *I. isarcica* zones. In Wadi Bih we see the loss of

517   gastropods and bivalves at this point (*34*), however the full resolution of the second extinction

518   phase has not been confirmed at this locality. Therefore we identify a 10 m interval for EP2. In

519   order to complete the age model we set the mid-point of EP2 as 251.88 Ma based on the absolute

520   age for EP2 in Meishan (*2*).

521

1.3 Analytical methods

523   Carbon and oxygen isotope ratios were determined at Edinburgh University and University of

524   Graz using the preparation technique and measurement routine as detailed in (*19*). All carbonate

525   isotopic values are quoted in the conventional δ per mil (‰) notation relative to VPDB.

526   Calibration to international reference material was through NBS 19 and the reproducibility of

527   replicate analyses for reference material, standards (in-house) and carbonate samples was better

528   than ±0.05 ‰ for $\delta^{13}C$ and ±0.1 ‰ for $\delta^{18}O$ at one standard deviation. For a detailed discussion

529   of the C and O isotopic data see (*19*).

530   Boron isotope ratios were determined in the isotope geochemistry laboratory at the

531   University of Bremen (Department of Geosciences and MARUM-Center for Marine

532   Environmental Sciences) using a ThermoFisher Scientific TRITON Plus Thermal Ionization

533   Mass Spectrometer. The $n(^{11}B)/n(^{10}B)$ measurements were performed using negative thermal

534   ionization mass spectrometry (N-TIMS) following the method detailed in (*37*). For analyses, 10

535   mg of the sample powder was dissolved in 100 μl 1 N HCl for 24 h at 20°C and subsequently

536   centrifuged. 1 μl boron-free seawater emitter (*38*) together with 1 μl of the sample solution

537   containing ~1 ng B were placed and dried on a degassed Re single filament. Analyses were

538   carried out at filament temperatures of 970°-1050°C. Boron isotopes were registered as BO_2^-

539   complexes on masses 42 and 43, and measurements were carried out at ion beam intensity of ~

540   10 pA on mass 43. Each sample measurement involved up to 200 blocks with 10 cycles each,

541   taking about 2 hours of data acquisition. B isotope ratios are given relative to NIST SRM 951 in

542   the conventional $\delta^{11}B$ (‰) notation. The external reproducibility of the certified reference

543   material NIST SRM 951 showed an $n(^{11}B)/n(^{10}B)$ ratio of 4.0065±0.0017 (2σ = 0.42‰, n=23)

544   over a period of 6 month of sample analyses. The long term (18 month) reproducibility is

545   4.0066±0.0018 (2σ = 0.44‰, n=58). The $n(^{11}B)/n(^{10}B)$ ratio of the reference material for each

546   analytical session was reproduced better than 0.6‰ (2σ). In addition to the NIST material, the

547   standard material M93-TB-FC-1, a *Porites* coral with a published value of 24.8±0.4‰ (2σ_mean),

548   as determined by different multicollector techniques (*39*) was also regularly analysed. The coral

549   replicates gave $\delta^{11}B$ values of 24.1±0.7‰ (2σ, n=16). Each sample solution was as a minimum

550   run in full duplicate and the uncertainty of the reference material was propagated into the

551   external uncertainty (2σ) on the isotope ratio of the sample (2σ*f*; Table S1). For further

552   information on the preparation and analytical methods see (*40*).

553

554   **2. Sample Selection**

555   A critical issue in using the B isotope composition of Permo-Triassic carbonate rocks for

556   reconstruction of ocean pH is the potential overprinting of the original isotope signal via

557   alteration. To obtain high-quality samples in which primary B isotope signals are still preserved,

558   we applied the sample selection procedures successfully used on Neoproterozoic carbonate rocks

559   to reconstruct Cryogenian and Ediacaran ocean pH variation *(37, 40, 41)*. In brief, samples

560   selected for isotope analyses were screened macroscopic (in the field), microscopic (scanning

561   electron microscope) and geochemically (carbon and oxygen isotopes), and selected because of

562 their uniformity in texture, absence of late stage secondary alteration and no correlation between

563 carbon and boron with oxygen isotopic signatures (Figs. S1 and S2).

564 The PTB interval itself was thought to occur in a regional cross-bedded ooid grainstone,

565 however, reconsideration of published thin-section images (*34*) (Fig S1 samples from WSA

566 transect, 0611300847 and 0611181243) demonstrate these are in fact microspheres (a.k.a

567 calcispheres). This fabric is unusual for the Phanerozoic but appears to represent supersaturated

568 conditions and these are thought to be primary spar precipitates (*42*).

569 To gain the highest potential for recording a primary boron signature we microdrilled

570 areas of pure micrite from micritc mudstones and micritised calcisphere grainstones where there

571 was no micro-optical evidence for veining, fracturing, clay minerals or bioclastic material.

572 Samples containing evidence of late stage secondary alteration or recrystallization, i.e. any

573 spar/microspar, were discarded. Potential analyses of disseminated detrital material in the

574 carbonates was also checked through elevated Al, Si and Ba concentrations and showed either no

575 or only minor dissemination of clay. The low availability of bioclastic material in this interval,

576 due to the extinction, argues against the potential of trends being caused by vital effects. In

577 particular the calcisphere grainstones of the PTB interval are classed as an abiotic carbonate that

578 provides an excellent opportunity to record seawater $\delta^{11}B$ in the absence of vital effects.

579
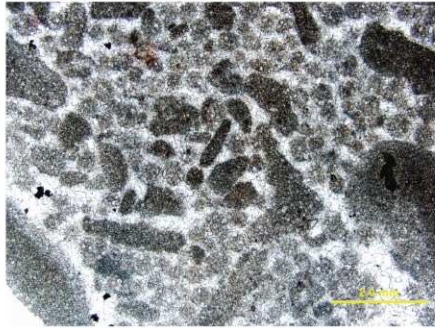
0611301104 (87m) WSA1 (91m)
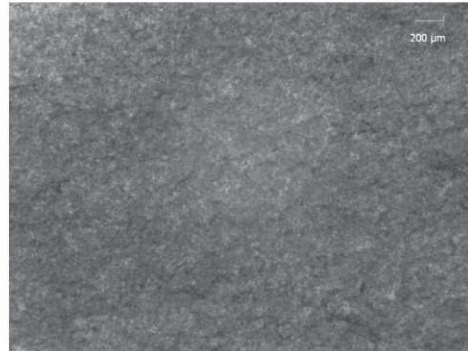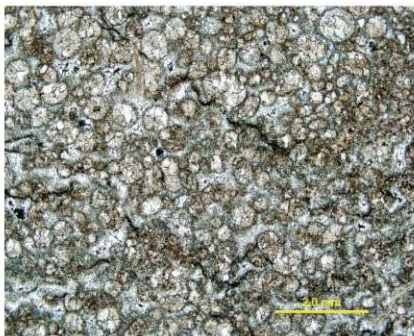
0611300847 (77m) WSA2 (86m)
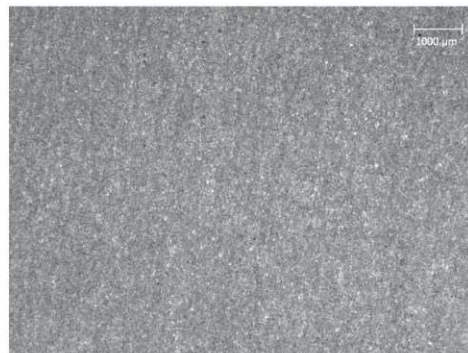
0611181243 (56m) WSA3 (85m)

580
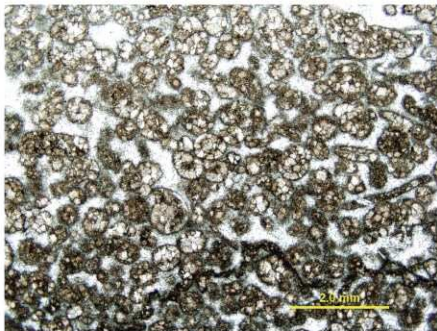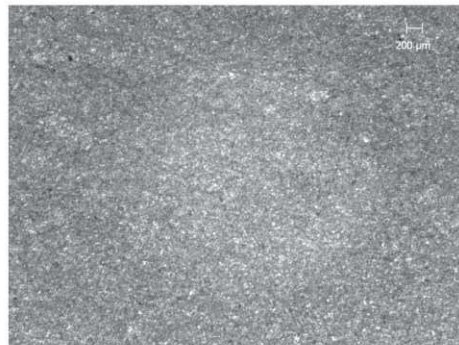
Fig S1: Examples of thin section images for the Wadi Bih section, WSA transect. WSA samples demonstrate homogeneous micritic texture of samples used for $\delta^{11}B$ analysis. 06- samples are from Maurer et al., (*34*) illustrating grainstones. The lack of compaction of grains and pore filling equant spar cements indicate very early/syn-sedimentary cementation. This fabric is consistent with indicators for supersaturated conditions in this interval, including thrombolites and flat pebble conglomerates, and suggests preservation of the original depositional fabric. Sample heights (m) as in Fig. 2 and Table S1.

588
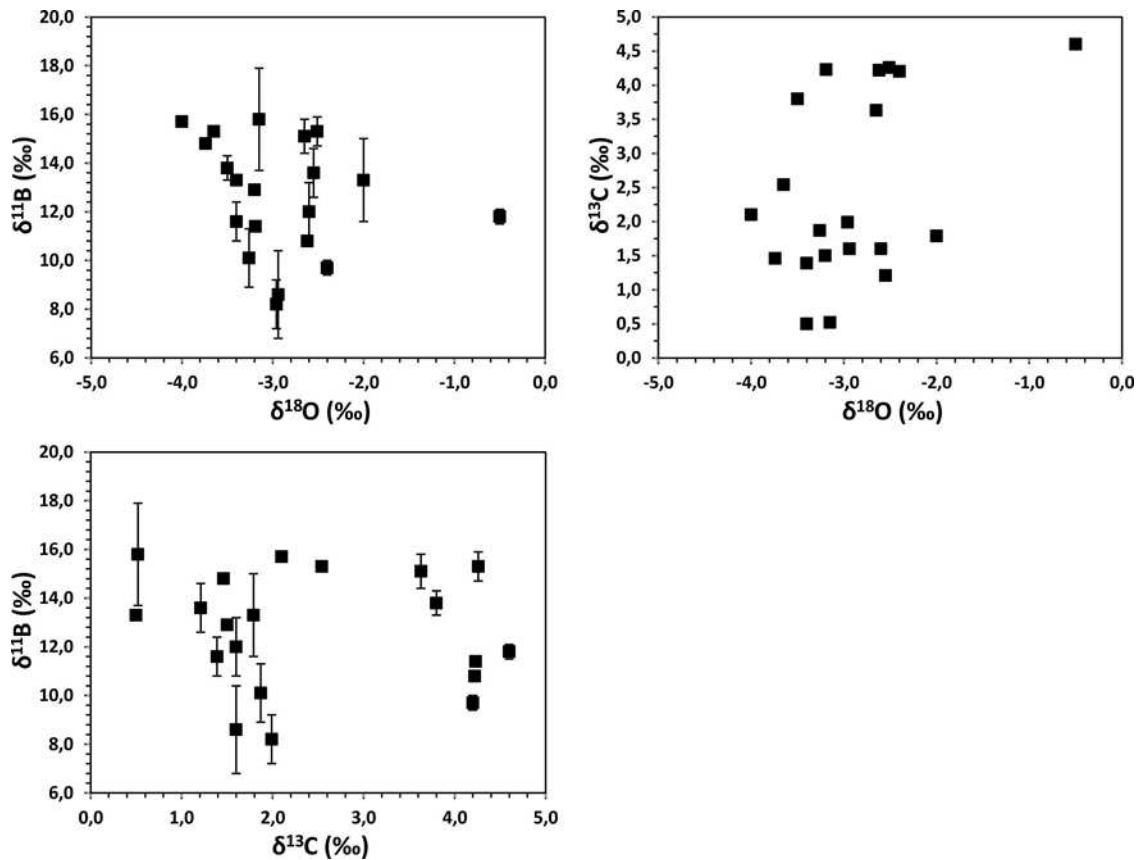
Fig S2: Cross-plots of boron, carbon, and oxygen isotope data for the marine carbonate samples from the Wadi Bih section. No significant correlation can be observed.

591

2.1 Diagenetic Influences

The PTB interval grainstone is composed of microspheres (a.k.a calcispheres). Microspheres are micritized and cemented with coarse equant spar cement (Fig S1). The lack of compaction of the microspheres suggests that the spar cement was extremely early and probably syn-sedimentary. This is a feature of other grainstones throughout this interval (WSA transect, sample 0611301104). Critically the presence of such well cemented fabrics in the grainstones of this interval would have prevented later stage fluid migration, and hence any late stage dolomitization. The total negative boron isotope excursion at EP2 is recorded across a numberof fabrics and facies, including micrite and the early cemented grainstones. Petrographic analysis

601   shows the extreme of the acidification event is recorded in fine-grained micrite where textures

602   are very homogenous samples WSA 1, 1B, 2, and 2A (Fig. S1).

603   Dolomitization in the Wadi Bih section is observed *(14)*, and occurred in two phases

604   where the first phase was fabric retentive syn-sedimentary dolomitization. The second phase of

605   dolomitization leads to the recrystallization of facies where near depositional porosity and

606   permeability had been maintained, i.e. preferentially in non-cemented grainstones. Neither of

607   these phases is classed as deep burial dolomitization (as confirmed by petrography in Figure S1

608   and the $\delta^{18}O$ data, Table S1). In the Musandam Peninsula the impact of dolomitization on carbon

609   and oxygen isotopes can be seen only in the close proximity to regional faults that provided high

610   permeability pathways for late burial dolomitizing fluids *(43)*, which were avoided for this study.

611   Diagenetic effects were also checked with geochemical tests for selected trace element

612   analyses, using secondary ionisation mass spectrometer Cameca ims 4f at the University of

613   Edinburgh. Diagenetic alteration was explored via Mn/Sr, which is often used as a geochemical

614   indicator of alteration and meteoric diagenesis in ancient carbonates *(44)*. While low Mn/Sr has

615   been found in ancient carbonates where there is clear optical evidence for recrystallization *(45)*,

616   high Mn/Sr may indicate carbonate precipitation from anoxic waters. In the selected samples,

617   Mn concentration is < 300 μg g^{-1}, Sr concentration ranges from 140 to 1400 μg g^{-1}, and the

618   Mn/Sr ratio is low (< 2), so suggesting no influence of meteoric fluids. The boron concentration

619   for the carbonate rocks is, on average, 1 μg g^{-1} and ranges between 0.2 and 1.7 μg g^{-1}.

620   Post-depositional alteration, especially meteoric diagenesis and recrystallization, is

621   assumed to decrease the isotopic composition of oxygen, boron and carbon isotopes (e.g. *46-48*).

622   Our selected carbonate samples show the distinct carbon isotope trend found at every PTB

623   section globally and $\delta^{18}O$ values ranging between -0.5 and -4.0‰, indicating no significant deep

624 burial alteration. All carbon and oxygen isotope data are given in Table S1. No statistically

625 significant correlation between carbon, oxygen and boron isotope data can be observed in our

626 data (Fig. S2).

627   The replication of the δ^{11}B across two complementary transects further support the

628 preservation of a primary seawater isotope signature as late stage dolomitization is expected to

629 be highly laterally variable and disrupt the smooth trends seen in the data.

630

631 **3. Support for a primary Boron isotope signature**

632 *3.1 Published δ^{11}B data*

633 So far, δ^{11}B data for Triassic carbonates have not been published and only limited δ^{11}B data,

634 based on low-Mg calcite brachiopod calcite from Oman (Saiwan Fm.), are available for the

635 Permian (Late Sakmarian). Keeping in mind the modern residence time of boron ($\tau \sim$14 to 20 Ma

636 *(47, 49)*, it is important to note that the range in δ^{11}B values (10.9±0.9‰ (1σ, n=4), 252.05-

637 252.15 Ma, mid-Changhsingian) overlap with the range in δ^{11}B values between 10.1 and 11.7‰

638 of the 285 Ma old brachiopod carbonates (average 10.6±0.‰, 1σ, n=5, *(16)*), which support the

639 primary nature of our boron isotope data.

640

641 *3.2 Environmental controls on the boron isotope composition*

642 The speciation of boron in seawater is predominantly pH dependent with minor controls from

643 temperature, salinity and pressure *(50)*. In our model we consider a dynamic temperature effect

644 on pK_B to calculate the pH of the seawater from the boron isotope composition preserved in

645 Permo-Triassic carbonate (see SM 4 and 5) however below we evaluate geological evidence to

646 consider whether these variables could drive the trends seen in our data.

647   *3.2.1* Temperature

648   Oxygen isotope data preserved in conodont apatite and low-Mg calcite brachiopods from

649   Permian-Triassic sections in Iran document tropical sea surface temperatures (SST) of 27–33°C

650   during the Changhsingian with a negative shift in $\delta^{18}O$ starting at the extinction horizon,

651   translating into a warming of SSTs to well over 35°C in the mid-Griesbachian (*51*). The results

652   are consistent with SSTs of the South Chinese sections, where a rapid increase in seawater

653   temperature from about 25° to 36°C across the Permian-Triassic section was proposed based on

654   conodont apatite (*6*). Since the dissociation constant of boric acid (pK_B) decreases with

655   increasing temperature (*50*), the proposed increase in SST could drive an increase in the B

656   isotope composition of the carbonates precipitated at the time of global warming and imply an

657   increase in ocean pH, even if ocean pH stayed stable. Using the pK_B data from (*50*), the potential

658   increase in SST at a given pH of 8 would drive an increase in $\delta^{11}B$ of the carbonates by 2‰ and

659   generate an artificial increase of < 0.2 pH units. Consequently, it could be argued that our

660   calculated pH variations are in essence the result of an increase in sea surface temperatures.

661   However, the oxygen isotope pattern (*51*) shows a continuous increase in temperatures across the

662   Permian-Triassic boundary and a thermal maximum in the mid-Griesbachian (~251.85 Ma).

663   Instead our data show a sharp increase in $\delta^{11}B$ and ocean pH in the Late Permian, well before the

664   increase in temperatures at EP1. The slight variability in $\delta^{11}B$ above the PTB, however, could be

665   driven by temperature variations.

666

667

668

669

670   *3.2.2 Salinity*

671   Similar to temperature, the pK_B is sensitive to salinity and increases with decreasing salinity (*52*).

672   To drive significant salinity-associated isotope variations across the Permo-Triassic boundary,

673   drastic changes in salinity (e.g. down to 25 psu compared to 35 psu) would be necessary.

674   However, even if modelled sea surface salinity values for the late Permian indicate generally

675   more saline conditions than present day (*52)*, sea surface salinity values for e.g. Iran and South

676   China still range between 34 and 35 psu (*51)* and will not have a significant effect on our pH

677   calculation. These samples come from an exclusively shallow water environment far from any

678   freshwater input, and so decreases in salinity would not affect our pH interpretations. The

679   depositional environment here ranges between open water ooid shoals to open and restricted

680   lagoon settings, which results in cyclic deposition on the scale of 5m. A shift toward more

681   restricted settings could drive increases in salinity that would affect the $\delta^{11}B$ record; however,

682   these depositional cycles are not on the same scale as the secular trends seen in $\delta^{11}B$.

683

684   *3.2.3 Water Depth*

685   Permo-Triassic seawater pH values have been reconstructed assuming carbonate precipitation at

686   sea surface conditions. Modern bathymetric pH and temperature profiles from the tropics show

687   that pH can decrease by up to ~0.2 units and temperature can drop by 15°C in the first 300 m

688   (*53*). Thus the B isotope composition of carbonates precipitated at greater water depths would be

689   more negative compared to surface precipitates. This potential depth effect is thought to be of

690   minimal influence to the Wadi Bih carbonates due to the exclusively shallow marine (subtidal to

691   intertidal) nature of the succession.

692   Consequently, uncertainties in the δ^{11}B-ocean pH relationship potentially introduced by

693   changes in temperature, salinity, bathymetry or biofacies would not be able to produce the

694   observed B isotope pattern with the sharp increase in the mid-Changhsingian (~252.04 Ma) and

695   the temporary decrease in the mid-Griesbachian (~251.88 Ma), but would be capable of

696   explaining some of the slight variations across the PTB.

697

698   **4. Boron-pH calculations**

699   The boron isotope composition of marine carbonates is used to reconstruct seawater pH values

700   and atmospheric pCO$_2$ concentrations (e.g. *54-58*). The application of the B isotope system as a

701   proxy for ocean pH is based on the observation that the fractionation factor for isotope exchange

702   between the two different speciation of boron (B(OH)$_3$ and B(OH)$_4^-$) is pH sensitive and

703   produces significant and traceable changes in the isotopic composition of carbonates (e.g. *57*).

704   The carbonate-associated boron isotopic composition δ^{11}B$_{carb}$ is assumed to be equal to

705   that of seawater B(OH)$_4^-$. The isotopic composition of the two boron species B(OH)$_4^-$ and

706   B(OH)$_3$ is determined by the isotopic fractionation factor α_{B3-B4} = 1.0272 (*59*), the speciation (a

707   strong function of pH, with smaller dependencies on temperature, pressure and salinity), and the

708   overall isotopic composition of seawater δ^{11}B$_{sw}$. The relationship between pH and δ^{11}B$_{carb}$ is

709   given by:

$$pH = pK_B - \log\left[- \frac{\delta^{11}B_{SW} - \delta^{11}B_{carb}}{\delta^{11}B_{SW} - \alpha_{B3-B4} \cdot \delta^{11}B_{carb} - 1000 \cdot (\alpha_{B3-B4} - 1)} \right]$$

710

711   where the effective dissociation constant pK_B includes the temperature, pressure and salinity

712   dependence. We dynamically calculate pK_B using CO2SYS-MATLAB v1.1 (*60*) (detailed in SM

713   5), which is consistent with the calculation and constants used by (*61*).

714   A prerequisite for reconstruction of past ocean pH values via B isotope data is the

715   knowledge of the primary B isotope composition $\delta^{11}B_{SW}$ of the ambient seawater. The B isotope

716   composition of modern seawater is regarded as being homogeneous with a $\delta^{11}B$ value of 39.5‰

717   (54). However, recent work on Precambrian to Phanerozoic carbonates and evaporites has shown

718   that the B isotope composition of seawater was highly variable in the geological past (16, 45, 46)

719   driven mainly by variations in the global boron budget during Earth history (23), exceeding the

720   residence time of B in seawater. Permo-Triassic seawater have been calculated based on changes

721   in processes controlling the oceanic boron budget, e.g. oceanic crust production rate and

722   continental boron flux (16) and suggests $\delta^{11}B_{SW}$ values of ~38‰ for the early Permian (285 Ma,

723   Late Sakmarian) and ~34‰ just before the PTB (16).

724   Given this uncertainty in $\delta^{11}B_{SW}$, we consider a range of values, determined by the

725   overall consistency of the $\delta^{11}B_{carb}$ data with model-derived constraints on the seawater carbonate

726   chemistry and hence pH, resulting in an envelope for the pH calculation. The model scenarios

727   encompass the range of previous estimates for background Early Permian conditions (13), which

728   suggest either high pCO_2 with lower pH (CO$_2$Hi: ~10 PAL, pH ~7.5), or low pCO_2 with higher

729   pH (CO$_2$Lo: ~3 PAL, pH ~8). In our model we consider these two scenarios with corresponding

730   seawater boron isotopic composition ($\delta^{11}B_{SW}$ = 34‰ and 36.8‰) required to reproduce the

731   observed $\delta^{11}B_{carb}$ (see SM Section 6 for further details of the model scenarios).

732   We illustrate the effect of uncertainties in $\delta^{11}B_{SW}$ and temperature on pH, and the overall

733   consistency with the $\delta^{11}B_{carb}$ data in Figure S3 and Table S1 (note that the full model described

734   in SM 4 also includes a dynamic calculation of temperature). The lowest $\delta^{11}B_{SW}$ =34‰ and

735   highest pH considered (scenario CO$_2$Lo) is effectively constrained by the model limitation on the

736   highest pH values immediately prior to EP1. The highest $\delta^{11}B_{SW}$ =36.8‰ and lowest pH

737   (scenario CO_2Hi) is effectively constrained by the limit of propagated uncertainty ($2\sigma f$) on the

738   lowest observed $\delta^{11}B_{carb}$ combined with the non-linearity of the B isotope system.

739   An additional uncertainty in interpreting $\delta^{11}B_{carb}$ is introduced by any potential offset or

740   fractionation between seawater borate $\delta^{11}B(OH)_4^-$ and $\delta^{11}B_{carb}$. As shown by (59), the laboratory

741   measured fractionation of abiotic carbonate (61) shows both an offset relative to that of the

742   artificial seawater, and a shallower slope with increasing pH. As we consider $\delta^{11}B_{SW}$ as a model

743   parameter to be determined, an overall offset is effectively subsumed within this. However a

744   shallower slope than that used here ($^{11-10}K_B$ = 1.0272 [ref 59], cf the one given for inorganic

745   carbonates (1.0267; [ref 62])) would require a larger pH change for a given observed change in

746    $\delta^{11}B_{carb.}$. Sanyal et al. (63) published B isotope values for inorganic calcite precipitates at three

747   different pH conditions - 7.9, 8.3, and 8.6. This same experimental inorganic calcite data and

748   associated estimates of $^{11-10}K_B$ in seawater were also presented by Klochko et al. (59, 64). To

749   date, there is no agreement as to the actual deviation of Sanyal's data (63) from the now

750   generally-accepted empirical fractionation factor given by Klochko et al (59). A best fit value of

751   1.0267 for the inorganic calcite precipitation was given by Pagani et al. (62). But by contrast, the

752   deviation between the inorganic carbonate values and the empirical fractionation appears much

753   bigger in Klochko et al. (59) and the best-fit value is given as 1.0260. This increased deviation is

754   explained by the difference in pH scale between natural or artificial seawater used for the

755   calibration experiments, and the experimental seawater pH measured on the (freshwater) NBS

756   scale. Klochko et al. (64) tries to address the deviations in $\delta^{11}B$ of inorganic precipitates from

757   empirical calibration studies and concludes that boric acid incorporation may contribute to the

758   ^{11}B enrichment observed in inorganic precipitates, especially at lower pH. They point out,

759   however, that all carbonates precipitated under controlled pH conditions were enriched in [11]B

760   relative to seawater borate (*63*).

761   If we use the best fit value (1.0267) given by Pagani et al. (*62*) for the inorganic

762   carbonates (Sanyal et al 2000) instead of the empirical value of Klochko et al. (*59*), then the

763   offset for the majority of the data would be around 0.05 pH units. Visible changes to more acidic

764   values would only appear at the lowermost pH estimates, but would still be less than 0.2 pH units

765   and fall within the general uncertainty. If we take the 1.026 value, the offset would generally

766   increase between ≤0.1 and 0.2 (pH range between ~8.4 and 7.8) but would indeed result in

767   significantly lower pH values of up to 0.5 units for the acidification event.

768   Given the limited amount of experimental inorganic calcite data and this disagreement

769   between the best-fit values, we have taken the simplest approach for the model representation

770   and chosen to use the most generally-accepted empirical fraction factor given by Klochko et al.

771   (*59*).

772

773
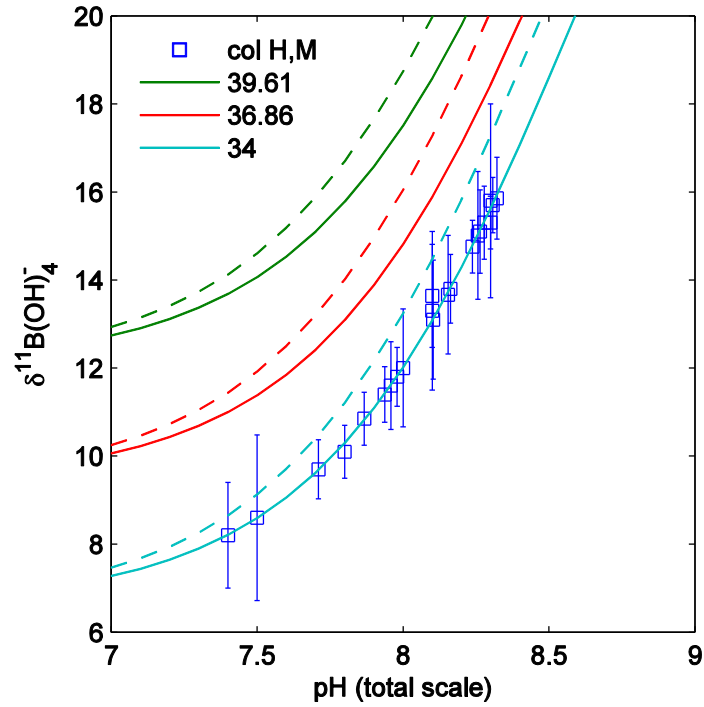
Figure S3 Effect of background $\delta^{11}B_{SW}$ and temperature on relationship between $\delta^{11}B_{carb}$ and pH
(total scale), for conditions appropriate to low-latitude surface ocean (atmospheric pressure,
salinity 35 psu, temperature 25°C (solid lines) and 35°C (dashed lines)). Three values are shown for
$\delta^{11}B_{SW}$: 39.61‰ (the contemporary value) and two values consistent with the end Permian data.
Data points and $2\sigma f$ errors are overlaid for the $\delta^{11}B_{SW}$ 34‰ case.

779

5. Model Description

5.1 Overview

The overall model structure (shown in Figure S4) is essentially a superset of carbon cycle models previously applied to the end Permian (*65, 66, 67)*, with additional consideration of the marine sulphur cycle. The model includes a three box ocean model as the minimum needed to demonstrate the effect of the biological pump on vertical DIC gradients and ocean redox state. The model is implemented as a set of coupled differential equations for the time evolution of reservoirs (Table S3), exchanging fluxes according to air-sea exchange, ocean circulation, applied external forcings and perturbations, and the biogeochemical processes described in Table S5. Model constants are defined in Table S4. The model implements an open inorganic carbon cycle, with atmospheric pCO$_2$ and marine DIC and Alk determined by the feedbacks between land-surface carbonate and silicate weathering and marine carbonate deposition. Oxidative weathering, volcanic degassing, and land and marine organic carbon burial are specified as forcings, as is marine phosphorus and hence productivity.
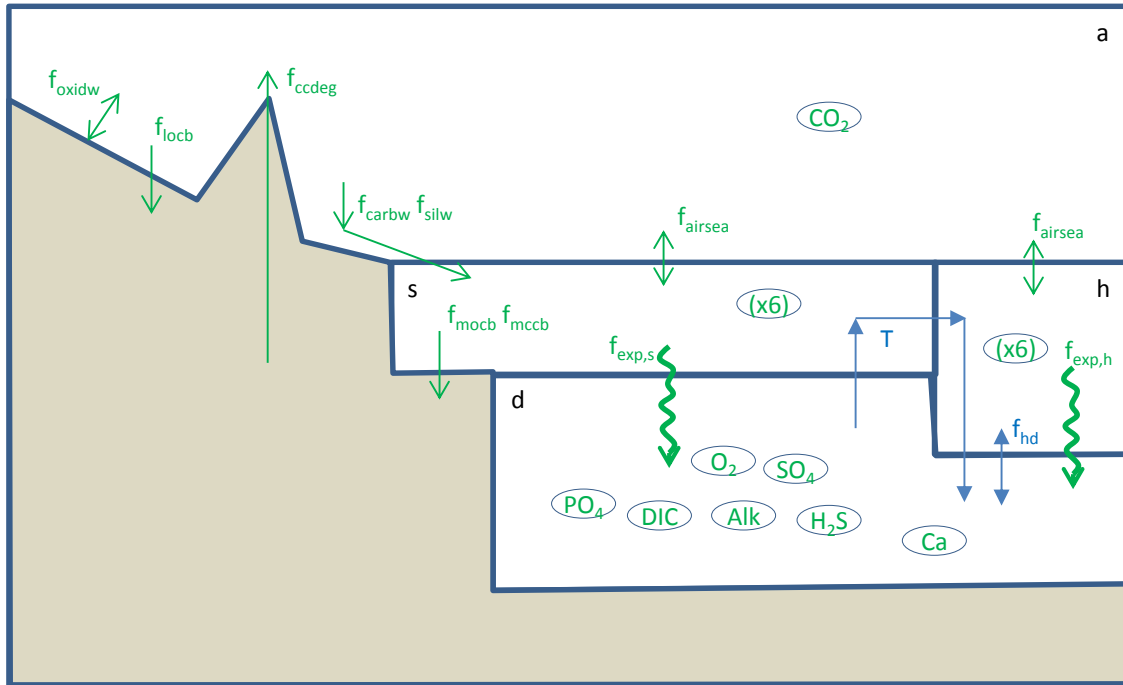
Figure S4 Model schematic. Ocean is represented by three boxes (s, h, d), with well-mixed atmosphere box a. Biogeochemical fluxes are shown in green, ocean circulation in blue. Biogeochemical reservoirs are shown as ovals.

795

796   Table S3 Model reservoirs

Reservoir	Initial size	Description
Atmosphere		
CO_2	eqb[a]	Atmospheric CO_2
Ocean		
$DIC_{(s,h,d)}$	eqb[a]	Total carbon
$Alk_{(s,h,d)}$	eqb[a]	Total alkalinity
$O_{2(s,h,d)}$	eqb[a]	Oxygen
$PO_{4(s,h,d)}$	2.15 μM / kg-sw	Phosphate
$SO_{4(s,h,d)}$	28 mM / kg-sw	Sulphate
$H_2S_{(s,h,d)}$	0	Sulphide
Ca	10.28 mM / kg-sw	Calcium (single reservoir)

797

798 Table S4 Model fluxes, constants, and forcings.

Flux	Model Parameter	Value	Units	Description
crust/mantle				
f_{ccdeg}	k_{12_ccdeg}	varies[a]	mol CO_2 yr^{-1}	Degassing
land surface				
f_{carbw}	k_{14_carbw}	1.33×10^{13}	mol $CaCO_3$ yr^{-1}	Carbonate weatherability
f_{silw}	k_{silw}	varies[a]	mol "$CaSiO_3$" yr^{-1}	Silicate weatherability
f_{oxidw}	k_{17_oxidw}	varies[a]	mol C yr^{-1}	Oxidative weathering
f_{locb}	k_{5_locb}	5×10^{12}	mol C yr^{-1}	Land organic carbon burial
marine				
	$k_{0\_Asurf(s)}$ $k_{0\_Asurf(h)}$	$0.85 \times 3.6 \times 10^{14}$ $0.15 \times 3.6 \times 10^{14}$	m^2	Ocean surface area
	$k_{0\_vol(s)}$ $k_{0\_vol(h)}$ $k_{0\_vol(d)}$	3.06×10^{16} 1.35×10^{16} 1.60×10^{21}	m^3	Ocean volume
T	k_{0_circT}	20	Sv	Overturning circulation
f_{hd}	$k_{0\_circfhd}$	60	Sv	High latitude – deep exchange
	k_{piston}	0.3	m d^{-1}	Air-sea piston velocity
	$T_{0(s)}$ $T_{0(d)}$	$T_{mean} + 6.5$ $\max(T_{mean} - 12.5, 2.5)$		Ocean temperature
	k_{0_sal}	35	psu	Ocean salinity
	$r_{c:p}$	161		Redfield C:P ratio
	$r_{n:p}$	16		Redfield N:P ratio
f_{mccb}	$k_{carbsedshallow}$	varies[a]	mol $CaCO_3$ yr^{-1}	Marine carbonate burial
f_{mocb}	k_{2_mocb}	5×10^{12}	mol C yr^{-1}	Marine organic carbon burial

a parameters k_{silw}, k_{12_ccdeg}, $k_{carbsedshallow}$ are per-scenario external forcings.

799
800

Table S5 Biogeochemical processes

Flux	Biogeochemical transformation	Stoichiometry								Rate	Description
		$CO_{2(a)}$	DIC	Ca	O_2	P	H_2S	SO_4^{2-}	Alk		
	land surface										
f_{carbw}	$CO_2 + H_2O + CaCO_3 \rightarrow Ca^{2+} + 2HCO_3^-$	-1	2	1					2	Equation (S2)	Carbonate weathering
f_{silw}	$2CO_2 + H_2O + CaSiO_3 \rightarrow SiO_2 + Ca^{2+} + 2HCO_3^-$	-2	2	1					2	Equation (S1)	Silicate weathering
f_{oxidw}	$CH_2O + O_2 \rightarrow CO_2 + H_2O$	1	0	0					0	k_{17_oxidw}	Oxidative weathering
f_{locb}	$CO_2 + H_2O \rightarrow CH_2O + O_2$	-1	0	0					0	k_{5_locb}	Organic carbon burial
	marine										
f_{exp}	$CO_2 + H_2O + xP \rightarrow CH_2OP_x + O_2$		-1	0	$1+2r_{n:p}/r_{c:p}$	$-1/r_{c:p}$	0	0	$r_{n:p}/r_{c:p}$ [a]	see Section 3.2.4	Export production
	$CH_2OP_x + O_2 \rightarrow CO_2 + H_2O + xP$		1	0	$-1-2r_{n:p}/r_{c:p}$	$1/r_{c:p}$	0	0	$-r_{n:p}/r_{c:p}$ [a]	see Section 3.2.4	Aerobic remineralisation
	$CH_2OP_x + \frac{1}{2}SO_4^{2-} \rightarrow HCO_3^- + xP + \frac{1}{2}H_2S$		1	0	0	$1/r_{c:p}$	0.5	-0.5	1	see Section 3.2.4	Sulphate reduction
	$H_2S + 2O_2 \rightarrow SO_4^{2-} + 2H^+$		0	0	-2	0	-1	1	-2	see Section 3.2.4	Sulphide oxidation
f_{mccb}	$Ca^{2+} + HCO_3^- \rightarrow H^+ + CaCO_3$	-1	-1	0	0	0	0	0	-2	$k_{carbsedshallow}$ $\times(\Omega_{aragonite}-1)^{1.7}$	Carbonate deposition
	$2H_2S + Fe(OH)_3 \rightarrow FeS_2 + \frac{1}{2}H_2 + 3H_2O$		0	0	-0.5	0	-2	0	0		Pyrite formation and burial
f_{mocb}	$CO_2 + H_2O \rightarrow CH_2O + O_2$		-1	0	1	0	0	0	0	k_{2_mocb}	Organic carbon burial

[a] contribution from nitrate, assumed at Redfield ratio.

5.2 Detailed description

5.2.1 pCO$_2$ and temperature

Global mean temperature T$_{mean}$ is calculated from atmospheric pCO$_2$ using the energy balance model as in COPSE *(68, 69),* with solar insolation appropriate for 250 Mya. Marine temperature T$_{O(s,h,d)}$ is calculated from the global mean assuming a fixed high-low latitude temperature difference and minimum temperature of 2.5^{0}C, with T$_{O(s)}$=T$_{mean}$+6.5 ^{0}C and T$_{O(h,d)}$=max(T$_{mean}$-12.5,2.5) ^{0}C.

5.2.2 Land surface weathering, degassing, and organic carbon burial

Land surface weathering is essentially a stripped-down version of that in COPSE (*69*), with carbonate and silicate weathering included but sulphur weathering and the long-timescale sedimentary reservoirs for sulphur and carbon are omitted. Atmospheric oxygen is fixed at the present-day value. Silicate and carbonate weathering are controlled by atmospheric pCO$_2$ and temperature with functional forms:

$$f_{silw}=k_{silw}\, e^{0.090(T_{mean}-T_0)}[1 + 0.038(T_{mean} - T_0)]^{0.65}\left(\frac{2\ pCO_2}{1 + pCO_2}\right) \quad \text{(S1)}$$

$$f_{carbw}=k_{14\_carbw}\, [1 + 0.087(T_{mean} - T_0)]\ \left(\frac{2\ pCO_2}{1 + pCO_2}\right) \quad \text{(S2)}$$

where T$_0$=15 ^{0}C.

Atmospheric CO$_2$ is consumed, and carbon, alkalinity and calcium supplied to the ocean, according to the stoichiometry defined in Table S5. Volcanic degassing, oxidative weathering, and land organic carbon burial are prescribed as forcings.

613   *5.2.3 Marine circulation and air-sea exchange*

614   Marine circulation is defined by a thermohaline circulation T, and high-latitude – deep

615   exchange f_{hd}. The marine box model includes P, O, DIC, Alk, SO_4, H_2S as per-box prognostic

616   variables, along with DIC $\delta^{13}C$. Marine carbonate chemistry is calculated using a modified

617   version of CO2SYS-MATLAB v1.1 *(60)*, extended to include sulphide alkalinity using the

618   constants tabulated by *(70)*. Air-sea exchange of oxygen and CO_2 assume a fixed piston

619   velocity and temperature-dependent solubility.

620

621   *5.2.4 Marine productivity and burial*

622   Productivity and hence the biological pump are controlled by the marine phosphorus

623   circulation. Biomass is produced in the surface ocean boxes, and exported and remineralized

624   in the deep box according to the processes and stoichiometries defined in Table S5.

625   Productivity in the 's' box is specified to consume all phosphorus down to negligible

626   concentration. Productivity in the 'h' box is specified to consume a fraction 0.18 of input

627   phosphorus. Remineralization in the deep ocean box consumes oxygen down to a limiting

628   concentration of 1μM and thereafter reduces sulphate to sulphide.

629   Shallow-water carbonate deposition occurs in the 's' box only and is controlled by

630   aragonite saturation state and a parameter representing a combination of shelf area and

631   calcification effectiveness, ie a 'Neritic' ocean without pelagic calcifiers *(71)*, functional

632   form $k_{carbsedshallow}*(\Omega_{aragonite}-1)^{1.7}$. Ocean carbonate compensation is not included, on the basis

633   this will be small for a 'Neritan' ocean.

634   Marine organic carbon burial from the 's' box and pyrite burial from the 'd' box are

635   imposed as forcings. Given the uncertainties in controls on phosphorus input over the end-

636   Permian interval, the marine phosphorus cycle is semi-closed (i.e. weathering feedback on

637   phosphorus input is not included), with imposed perturbations (forcings) to source/sink

638   balance (riverine input vs burial) applied as inputs to the 's' box to control phosphorus

639   concentration.

640

641   *5.2.5 Carbon isotopes*

642   Carbon isotopes are implemented with additional reservoirs for each of atmospheric CO_2 and

643   marine $DIC_{(s,h,d)}$. Air-sea exchange fractionates according to the temperature-dependent

644   equilibrium and kinetic factors determined by Zhang et al. (*72*). Marine export production is

645   at fixed fractionation relative to DIC, with $\delta^{13}C_{exp(s,h)} = \delta^{13}DIC_{(s,h)}$ - 25 ‰.

646   Volcanic degassing, carbonate weathering, and oxidative weathering are assumed to

647   add carbon at fixed fractionations of -4.9‰, 2.65‰, and -25‰ respectively. Atmospheric

648   CO_2 consumed by silicate and carbonate weathering (and added to the ocean 's' box as DIC)

649   is fractionated relative to atmospheric CO_2 according to the freshwater fractionation of Zhang

650   et al. (*72*).

651   Land and marine organic carbon burial is at fixed fractionation relative to atmospheric

652   CO_2 and marine DIC, with $\delta^{13}C_{locb} = \delta^{13}CO_2$-19 ‰ and $\delta^{13}C_{mocb} = \delta^{13}DIC_{(s)}$-25 ‰. Marine

653   inorganic carbon burial is assumed to not fractionate relative to $DIC_{(s)}$.

654

655   *5.2.6 Boron isotopes*

656   Carbonate-associated boron isotopic composition $\delta^{11}B_{carb}$ is assumed to be equal to that of

657   seawater $B(OH)_4^-$. Speciation of $B(OH)_4^-$ and $B(OH)_3$ is calculated using CO2SYS-MATLAB

658   v1.1 (*60*). Isotopic composition is then calculated from speciation x_{bo4} = [$B(OH)_4^-$]/[B total]

659   and seawater $\delta^{11}B_{SW}$ as

$$\delta^{11}B_{carb} = \frac{\delta^{11}B_{sw} - 1000(1 - x_{bo4})(\alpha_B - 1)}{\alpha_B - x_{bo4}(\alpha_B - 1)}$$

660   with the isotopic fractionation factor $\alpha_B = 1.0272$.

661

662

5.2.7 Model spinup and steady state

The model pCO$_2$ steady-state is defined by the imposed degassing rate, organic carbon burial

and oxidation, and silicate weathering parameterisations, where these together define a

unique value for the steady-state atmospheric pCO2 and temperature where $f_{ccdeg}+f_{oxidw} =$

$f_{silw}+f_{locb}+f_{mocb}$. During spin-up, the ocean chemistry and hence atmosphere-ocean CO$_2$

partitioning adjust (on the silicate weathering timescale of ~100kyr) to a steady-state, with

the aragonite saturation state adjusting such that carbonate burial balances inputs from

carbonate and silicate weathering.

671

5.2.8 Sensitivity to seawater composition

The Mg and Ca composition of end-Permian seawater (as determined from fluid inclusions)

is consistent with that of modern seawater ([Mg] = 53 mmol/kg, [Ca] = 10.3 mmol/kg), but

with large uncertainties (*6*). Sulphate concentration may have been much lower than modern

values (*73, 74*). We estimate the uncertainties in carbonate system chemistry following the

approach of (*75*). We estimate the effect on K_1 and K_2 from model results (*74*) as:

$$\frac{K_1^*}{K_1} = 1 + 0.155\frac{\Delta[\text{Mg}^{2+}]}{[\text{Mg}^{2+}]_m} + 0.033\frac{\Delta[\text{Ca}^{2+}]}{[\text{Ca}^{2+}]_m} - 0.019\frac{\Delta[\text{SO}_4^{2-}]}{[\text{SO}_4^{2-}]_m}$$

$$\frac{K_2^*}{K_2} = 1 + 0.641\frac{\Delta[\text{Mg}^{2+}]}{[\text{Mg}^{2+}]_m} + 0.071\frac{\Delta[\text{Ca}^{2+}]}{[\text{Ca}^{2+}]_m} - 0.054\frac{\Delta[\text{SO}_4^{2-}]}{[\text{SO}_4^{2-}]_m}$$

where subscript m refers to modern values and an asterix to end-Permian values. Taking

extremal values [Mg^{2+}]*/[Mg]$_m$=0.5, [Ca^{2+}]*/[Ca]$_m$=2, [SO$^{2-}_4$]*/[SO$^{2-}_4$]$_m$=0.1, we have

K_1*/K_1=1-0.078+0.033+0.0171=0.972 or pK_1*=pK_1+0.012 (or for [Mg^{2+}] alone,

K_1*/K_1=0.92, pK_1*=pK_1+0.035). For a fixed pCO$_2$, this implies a corresponding decrease in

[HCO$_3^-$] and hence DIC inventory, or equivalently an increase in pH for the same DIC

content.   The   corresponding   effect   on K_2 is   much   larger, K_2*/K_2=1-

684   0.32+0.0171+0.049=0.75.We estimate the effect of Mg concentration on the calcite solubility

685   constant K_{sp} using the parameterisation given by (76) as:

$$\frac{K_{sp}^*}{K_{sp,m}} = 1 - 0.0833 \left(\frac{[\text{Mg}^{2+}]_m}{[\text{Ca}^{2+}]_m} - \frac{[\text{Mg}^{2+}]^*}{[\text{Ca}^{2+}]^*} \right)$$

686   which gives K_{sp}^*/K_{sp}=1-0.33.

687   This sensitivity study shows that the uncertainty in K_1 therefore introduces only a small

688   uncertainty in pH ($\sim< 0.03$) or equivalently a ~10% uncertainty in DIC inventory relative to

689   pCO_2. The combined uncertainties in K_2, K_{sp} and $[\text{Ca}^{2+}]$ are larger, introducing corresponding

690   uncertainties in calcite saturation state. However, within the model employed here, this is

691   effectively absorbed into a rescaling of the parameter $k_{carbsedshallow}$.

692

693   **6- Model Scenarios**

694   Given the uncertainty in the absolute value of the seawater boron isotope composition

695   (section S4), we consider two scenarios with initial steady-state conditions as in Table S6:

696   scenario CO_2Hi uses $\delta^{11}B_{SW}$=36.86, and CO_2Lo uses $\delta^{11}B_{SW}$=34. Here ocean pH depends on

697   the combination of atmospheric pCO_2 and carbonate saturation state. Atmospheric pCO_2 (set

698   by the ratio of net carbon sources : silicate weatherability) is tuned to 3 or 10 PAL,

699   encompassing the range of conditions considered by previous model studies (77, 78, 79).

700   Ocean carbonate saturation state is set by carbonate sedimentation efficiency parameter

701    $k_{carbsedshallow}$, which represents a combination of shelf area x deposition rate. A summary of

702   scenarios required to explain the three events in our $\delta^{11}B$ data are given in Table S7 and

703   explored in further detail below.

704

Table S6 Steady-state initial conditions summary

	CO$_2$Hi	CO$_2$Lo	Units	Description
Parameters				
k$_{12\_ccdeg}$	11.80x10^{12}	11.80x10^{12}	mol CO$_2$ yr^{-1}	degassing
k$_{17\_oxidw}$	5x10^{12}	5.92x10^{12}	mol C yr^{-1}	oxidative weathering
k$_{silw}$	2.40x10^{12}	6.60x10^{12}	mol CaSiO$_3$ yr^{-1}	Silicate weatherability
k$_{carbsedshallow}$	18.43x10^{12}	1.44x10^{12}	mol CaCO$_3$ yr^{-1}	Marine carbonate burial efficiency
Steady-state conditions				
pCO$_2$, ppm	2800	845		
T$_{mean}$	22.18	14.94	^{0}C	Global mean temp
T$_{O(s)}$	28.7	21.44	^{0}C	Ocean temp
$\Omega_{arag(s)}$	2.44	6.15		Aragonite saturation, 's' box
pH	7.51,7.46,7.07	8.02, 7.99, 7.60	Total scale	Ocean pH, 's','h','d'
DIC total	5.53x10^{18}	6.01x10^{18}	mol	
δ^{13}DIC$_{(s)}$	+3.32	+2.97	‰	
Fluxes				
f$_{carbw}$	27.46x10^{12}	15.58x10^{12}	mol CaCO$_3$ yr^{-1}	Carbonate weathering
f$_{silw}$	6.80x10^{12}	7.72x10^{12}	mol "CaSiO$_3$" yr^{-1}	Silicate weathering
f$_{ccdeg}$	11.80x10^{12}	11.80x10^{12}	mol CO$_2$ yr^{-1}	Degassing
f$_{mccb}$	34.26 x10^{12}	23.30x10^{12}	mol CaCO$_3$ yr^{-1}	Marine carbonate burial

Table S7 Overview of scenarios

Event	Time	Scenario	
		CO$_2$Hi	**CO$_2$Lo**
		$\delta^{11}B_{sw}$=36.86	$\delta^{11}B_{sw}$=34
pH rise	252.25 Ma	Marine productivity increase	
	252.05 Ma	Carbonate sedimentation efficiency decrease	
		Pyrite deposition, Carbonate weathering increase	
δ^{13}C drop, stable pH	252.00 Ma	Land organic carbon burial decrease	
	251.95 Ma	Slow (~50kyr) isotopically light carbon addition.	
Acidification, no δ^{13}C change	251.88 Ma	Rapid (10kyr) isotopically heavy carbon addition	

708

709

6.1 Mechanisms for pH rise

The rise in δ^{11}B at 252.05 Ma corresponds to a rise in pH from 7.5 to 8.0 for scenario CO$_2$Hi,

and from 8.0 to 8.3 for scenario CO$_2$Lo. Given the major upheavals in the Earth system at the

end-Permian, multiple mechanisms including changes in silicate and carbonate weathering,

and marine changes in calcification and due to anoxia may potentially contribute to pH rise,

and we use model sensitivity studies to determine potential constraints. We first review

evidence for each mechanism, then summarize the model sensitivity studies and propose

plausible scenarios involving multiple drivers.

6.1.1 Carbonate weathering

The overall high weathering rates across the Permian-Triassic boundary also imply an increase in carbonate weathering, possibly combined with any direct effect from chemical weathering of eroded clastic material itself.

There is also direct evidence for later sea-level regression and subaerial weathering of the shallowest sections of the S. China carbonate platform, coincident with EP1 *(20)* which may contribute to maintaining pH over this interval. To estimate an order of magnitude for enhanced carbonate shelf weathering: 10^{18} mol $CaCO_3$, density 2.8 g cm^{-3} has volume 36,000 km^3, or 100m x $3.6 \times 10^5 km^2$, or 1800km of 200km wide shelf; this would provide a weathering flux of 10^{13} mol $CaCO_3$ yr^{-1} for 100 kyr, comparable to the background carbonate weathering rate.

6.1.2 Decrease in calcification effectiveness

Overall global biotic calcification effectiveness is determined by the combination of available shelf area, and local ecosystem-dependent rates. A reduction in area of deposition could be because anoxic/euxinic waters extend onto the shelf bottom precluding those parts from hosting deposition, and/or because there is a sea level change reducing shelf area. The input of clastics prior to EP1 could also reduce carbonate production as a result of ecosystem impacts (*80, 81*).

6.1.3 Productivity-driven ocean anoxia, sulphate reduction, and pyrite burial

Multiple lines of evidence suggest a (large) expansion of oxygen minimum zones prior to the PT boundary, while the deep ocean remains suboxic. These include U isotope evidence for ~6x increase in anoxic fraction (*82)*, extensive pyrite deposition (*83*), and GCM studies (*84*) illustrating the spatial distribution of anoxia.

741   We represent productivity-driven ocean anoxia by increasing marine phosphorus from

742   the present-day value to 2.3x present (the value used by (*66*). This is achieved by adding

743   phosphorus to the marine 's' reservoir (representing a net excess of riverine input over

744   sediment output) at rate $3.9x10^{10}$ mol yr^{-1} over the interval 252.15 – 252.05 Ma (cf present-

745   day riverine input $\approx 2x10^{10}$ mol yr^{-1}) (*64*). This results in pCO$_2$ drawdown as a result of the

746   increased biological pump, and in sulphate reduction leading to ~ 50 μM H$_2$S in the 'd' box.

747   Note that sulphate reduction increases alkalinity / pH in the 'd' box by ΔpH ~ 0.1, but as the

748   S redox shuttle is completed by sulphide oxidation at the base of the oxic surface box, this

749   has no effect on the pH of the oxic surface ocean.

750   High rates of pyrite formation are seen at and before EP1 (*83, 85*). Pyrite burial

751   results in a net alkalinity source (*86*). We assume that pyrite deposition is a water-column

752   process, hence is limited by the availability of iron and sulphide. The most limiting factor for

753   the scenarios considered here is iron. To quantify this, we estimate pyrite deposition rate

754   sustainable over a timescale of ~100kyr as ~$1.25x10^{12}$ mol FeS$_2$ yr^{-1}, based on availability of

755   reactive iron Fe$_{HR}$ (in the contemporary oxic ocean, Fe$_{HR}$ total input to the ocean is ~ $6.8x10^{12}$

756   mol yr^{-1}, of which only ~$1.3x10^{12}$ mol yr^{-1} gets to the deep ocean (*87*). Sulphide availability

757   is determined by anaerobic organic carbon remineralisation in the 'd' box, which is a model-

758   determined fraction of total export production ~10^{14} mol yr^{-1}, and is less limiting than iron for

759   the scenarios considered here. This assumes that sulphate for remineralisation (and hence

760   sulphide availability) is unconstrained by marine sulphur availability, ie that the marine

761   sulphate reservoir is drawn down. This is supported by (or at least consistent with) the data

762   indicating low early Triassic marine sulphate, < 4mM (*75, 88*).

763

764   *6.1.4 Silicate weathering*

765   Anomalously high sediment fluxes across the Permian-Triassic boundary *(80, 81)* imply soil

766   loss and increased exposure of highly weatherable rock surfaces, with increases in both

767   physical and chemical weathering. Early Siberian traps emplacement and an increase in area

768   of weatherable basalt also may contribute to an increase in overall silicate weatherability. The

769   main increase in silicate weathering is seen in the Griesbachian but increases may have

770   accompanied the carbon injection for EP1.

771   *6.1.5 Combined scenarios*

772   We summarize the effect of illustrative perturbations for the separate contribution of each

773   potential driver of pH increase in Table S8. Perturbations were applied to the CO_2Lo steady

774   state at 251.95Ma (corresponding to the pH rise seen in the $\delta^{11}B$ data), with effect shown

775   100kyr later (at EP1).   The marine carbonate system responds on a timescale of ~10kyr,

776   hence reaches a steady state source-sink balance, however the timescale for land-surface

777   weathering feedbacks is >~100 kyr hence the system does not reach a steady state. The

778   dynamic response is included in the full scenarios.

779   As shown in figure S5, the perturbations fall into two groups. Increases in silicate

780   weatherability and pyrite deposition leave carbonate input rate and calcification output

781   essentially unchanged, hence result in changes to atmospheric pCO_2 at nearly constant

782   saturation state. Changes to atmospheric pCO_2 alone are unable to produce a change in pH or

783   $\delta^{11}B$ as large as that seen in the data without implausibly low pCO_2 and hence temperature,

784   hence these cannot be the sole drivers of pH increase. Reductions in calcification

785   effectiveness or increases in carbonate inputs change both the carbonate system saturation

786   state and atmospheric pCO_2, resulting in a much larger increase in pH for a given decrease in

787   pCO_2. A major contribution from either or both of these mechanisms is therefore required.

788   The results from the perturbations study demonstrate that all mechanisms may

789   contribute to pH rise, with a major contribution from either or both carbonate input and

790   decrease in calcification effectiveness required. Given the most likely case where multiple

791   mechanisms all contribute, we construct scenarios with a decrease in calcification

792   effectiveness as the major component and smaller contributions from pyrite burial and

793   carbonate weathering (Figure S6). The perturbations considered for the two scenarios are

794   summarized in Table S9 and the dynamic response is shown in Figure S6.
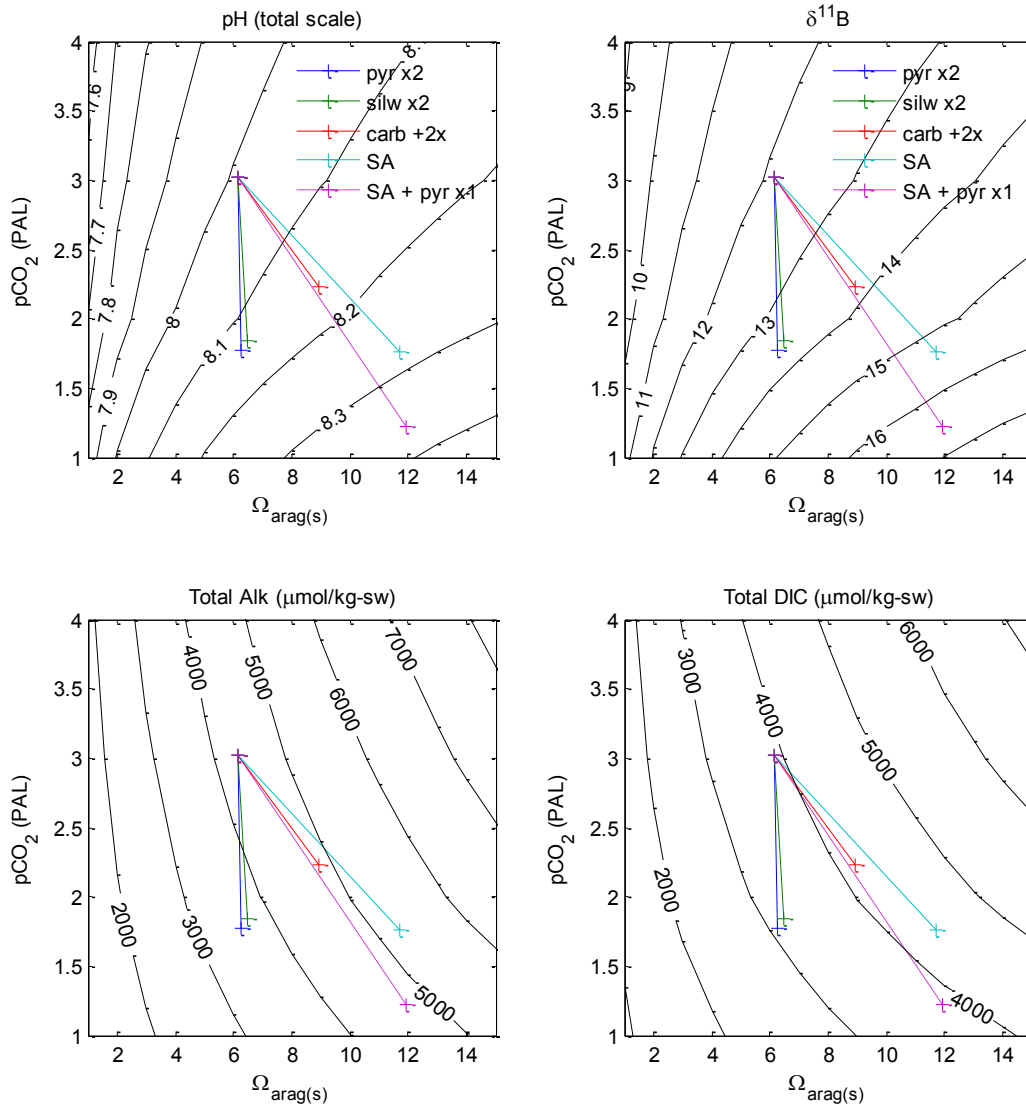
795

796

797

Figure S5 Effect of illustrative perturbations (defined in Table S8) on carbonate system properties for atmosphere and ocean surface (s) box. Contours show carbonate system parameters for a constant temperature of 25 °C, salinity 35 psu, pressure 1 atm, hence do not exactly correspond to the full model results with varying temperature.
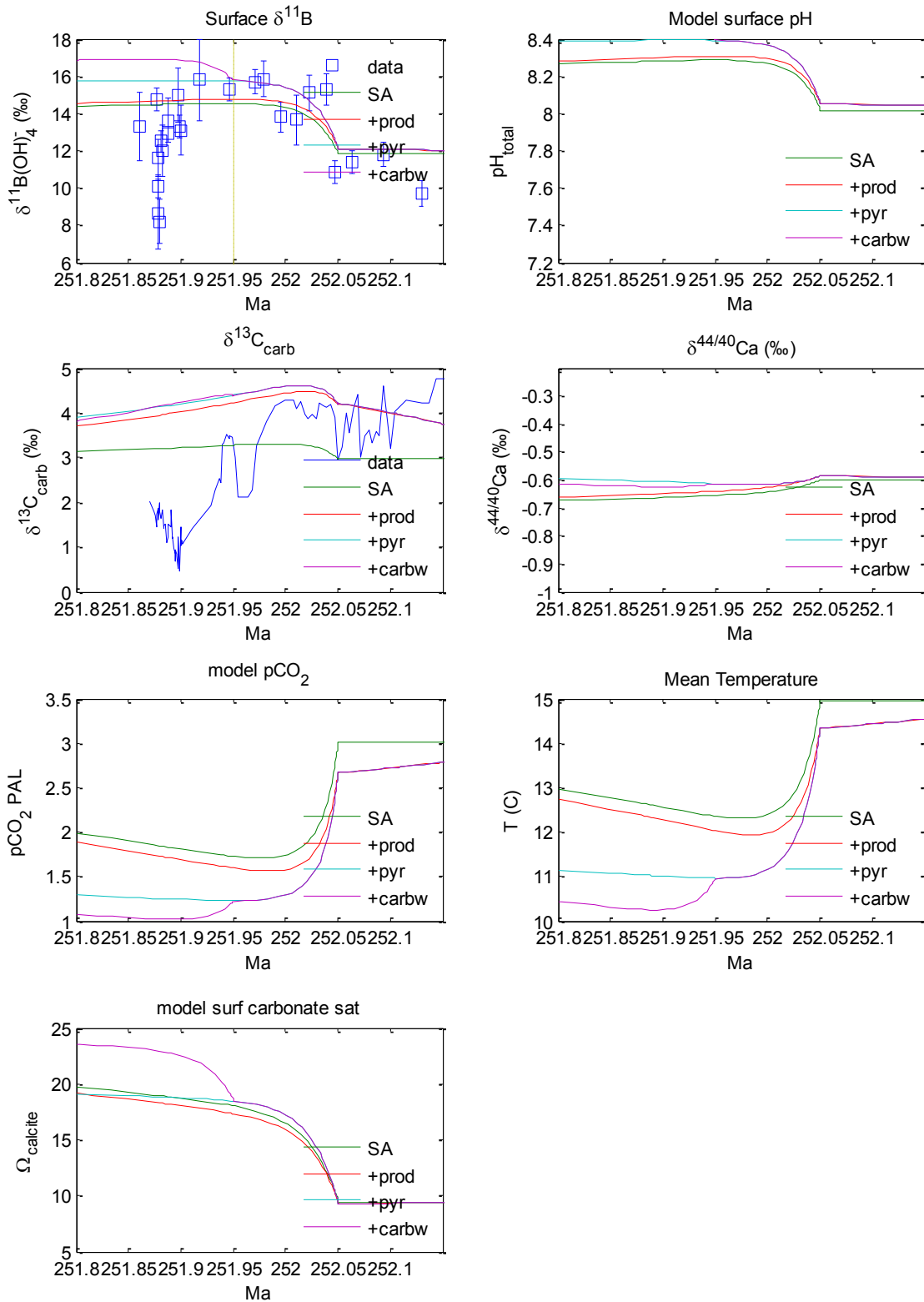
Figure S6 Scenario CO$_2$*Lo*: Contributions to pH increase. 'SA': effect of calcification effectiveness decrease. '+prod' effect of increased marine productivity and anoxia. '+pyr' pyrite burial, and '+carb' carbonate weathering

802

803 Table S8 Sensitivity study for pH rise mechanisms. Perturbations applied to steady-state CO_2Lo at 252.05Ma, effect shown at 251.95Ma.

Mechanism	Perturbation	$pH_{tot(s)}$	$\delta^{11}B_{(s)}$	$\Omega_{arag(s)}$	pCO_2	T_{mean}	Comments
steady-state CO_2Lo	none	8.02	11.83	6.15	845	14.94	**Error! Reference source not found.**
		Δ	Δ	Δ	Δ	Δ	
'calc eff' decrease	$k_{carbsedshallow}$ 14.4×10^{11} $\rightarrow$ 2.47×10^{11} (ie x 0.17)	+0.266	+2.72	+5.55	-351	-2.58	
	$k_{carbsedshallow}$ 14.4×10^{11} $\rightarrow$ 1.23×10^{11} (ie x 0.085)	+0.36	+3.78	+8.2	-446	-3.39	
pyr deposition	'x1': 1.25×10^{12} mol FeS_2 yr^{-1}	+0.083	+0.71	-0.03	-213	-1.39	
	'x2': 2.5×10^{12} mol FeS_2 yr^{-1}	+0.155	+1.36	+0.12	-347	-2.46	
	'x4': 5×10^{12} mol FeS_2 yr^{-1}	+0.318	+3.062	+0.46	-557	-4.66	~ upper limit from Fe availability
carb input	'+1x': add 15×10^{12} mol $CaCO_3$ yr^{-1}	+0.082	+0.77	+1.44	-130	-0.81	+1x = approx 2x background weathering rate. Ocean carb deposition rapidly compensates
	'+2x': add 30×10^{12} mol $CaCO_3$ yr^{-1}	+0.147	+1.41	+2.76	-219	-1.44	+2x = ~3x background weath rate
	'+3x': add 45×10^{12} mol $CaCO_3$ yr^{-1}	+0.20	+1.97	+3.99	-285	-1.94	+3x = ~4x background weath rate
silw weath increase	x2 k_{silw} $6.60\times10^{12}\rightarrow 13.2\times10^{12}$	+0.14	+1.19	+0.35	-329	-2.30	'Weatherability': drives pH primarily via pCO2 decrease
	x4 k_{silw} $6.60\times10^{12}\rightarrow 26.4\times10^{12}$	+0.32	+3.08	+0.57	-588	-5.09	
calc eff + pyr	$k_{carbsedshallow}$ 14.4×10^{11} -> 2.47×10^{11} 'x1': 1.25×10^{12} mol FeS_2 yr^{-1}	+0.37	+3.91	+5.78	-501	-3.98	used for Scenario *CO_2Lo*.
carb + pyr	'+2x': add 30×10^{12} mol $CaCO_3$ yr^{-1} 'x2': 2.5×10^{12} mol FeS_2 yr^{-1}	+0.28	+3.09	+2.92	-485	-3.79	

804

805

806   Table S9 Summary of pH rise mechanisms included in scenarios *CO₂Hi and CO₂Lo*

	CO₂Hi	*CO₂Lo*
Decrease in calcification effectiveness	$k_{carbsedshallow}$ decrease from 1.8433×10^{13} to 0.72×10^{12}	$k_{carbsedshallow}$ decrease from 1.44×10^{12} to 2.47×10^{11}
Productivity,anoxia	Increase P linearly to 2.3x, over interval 252.25 – 252.05 Ma	
Pyrite burial	1.25×10^{12} mol FeS_2 yr^{-1} starting at 252.05Ma	
Carbonate weathering	9.7×10^{12} mol/yr starting at 251.95Ma	

807

808

809

810   ***6.2 Sources of carbon and volatiles causing a negative $\delta^{13}C$ excursion or pH excursion***

811

812   *6.2.1 Terrestrial Carbon burial*

813   The effect of destruction of the land biota and a corresponding decline in land organic

814   carbon burial at the PT boundary was first considered by Broecker and Peacock (*89*). We

815   represent this by setting land organic carbon burial to zero at T=251.95Ma, resulting in a

816   drop in $\delta^{13}C_{carb}$ of $\approx$ 4‰ (comparable to that seen in end-Permian sections), but over

817   timescale of ~100kyr.

818

819   *6.2.2 Marine Carbon burial*

820   Despite (or because of) ecological shifts to a cyanobacteria dominated ecosystem (*3*), proxy

821   evidence for continued high sediment organic carbon fluxes (*84*) and a vertical $\delta^{13}C$

822   gradient (*92, 93*) as well as continuing marine anoxia suggests that high marine

823   productivity continues through Permian-Triassic. Interruption to the marine biological

824   pump would result in a short timescale (ocean circulation timescale ~10^3 yr) increase in

825   surface ocean pH and decrease in surface ocean (and hence carbonate) $\delta^{13}C$. This was

826   considered as a mechanism for short-timescale $\delta^{13}C$ fluctuations over the PT interval (*67*).

827   We do not consider this further here as this mechanism results in coupled perturbations to

828   both surface ocean pH and $\delta^{13}C$, and hence cannot be the major driver for the '$\delta^{13}C$ without

829   pH' or 'pH without $\delta^{13}C$' signals. Smaller perturbations (interruptions) to the biological

830   pump may be plausible as a contributor to short-timescale $\delta^{13}C$ signals following EP1.

831

832   *6.2.3 Siberian traps volcanism and contact metamorphism*

833   In order to bound plausible model scenarios, we review here potential mechanisms for

834   volatile input from the Siberian Traps and summarise constraints on magnitudes and rates,

835   based on (*24, 27, 93*).

836   The Siberian Traps magma area is estimated as $2.5 - 5\times10^6$ km^2 and volume >

837   2×10^6 km^3. This intruded into the Tungska sedimentary sequence, which reaches 12.5 km in

838   thickness and includes. $\approx$2.5 km of Cambrian evaporites containing abundant limestone,

839   halite, dolomite and anhydrite (*24, 27),* coal deposits, as well as Neo-Proterozoic

840   petroleum-bearing shale and carbonate. Intrusion of magma into the sediments resulted in

841   abundant sills and dykes with accompanying contact aureoles, and explosively-generated

842   pipes. The igneous province is estimated to contain approximately 50% intrusive dykes and

843   sills, 30% basalt lava flows, and 20% pyroclastic material (*94, 95*).

844   The volume of sediments affected by contact metamorphism is estimated (*27*) from

845   a sill area of 2×10^6 km^2, thickness 200m, generating a contact aureole of thickness 400m.

846   This results in potential release of $0.8\text{-}2.3\times10^{18}$ mol C (as isotopically light methane and

847   CO$_2$) from metamorphic degassing of organic carbon (assuming the TOC weight percent

848   reacted is $0.5 - 1.5\%$), over a timescale $\approx$50kyr. In addition, pipes (each with source region

849    $\approx$5 km^3) could release $0.1 - 0.3\times10^{18}$ mol C over $\approx$6.5 kyr. Intrusion into carbonates could

850   release comparable quantities of isotopically-heavy CO$_2$ via calcsilicate formation and

851   decarbonation of dolomite into periclase and calcite, and intrusion into anhydrite could

852   release comparable quantities of S as SO$_2$ (*96*). Interaction between petroleum-bearing

853   inclusions and host rock salt could in addition generate halocarbons, estimated at $1\text{-}3\times10^{17}$

854   mol CH$_3$Cl (*35*). Intrusion into coal-seams could result in explosive interaction resulting in

855   large-scale coal combustion (*93*).

856   The Siberian Traps magmas contain anomalously high quantities of S, Cl, F (*27*),

857   estimated to result in total intrusive and extrusive degassing of 0.2-0.25x10^{18} mol S, 0.1-

858   0.25 x10^{18} mol Cl, and 0.4-0.7 x10^{18} mol F (*31*). The ultimate source of these volatiles is

859   likely to be assimilation from sedimentary host rocks.

860

861   *6.2.4 Carbon injection perturbations*

862   Given the episodic nature and likely variability in isotopic composition of carbon additions

863   from Siberian Traps volcanism and contact metamorphism, we consider size, rate, and

864   isotopic composition of carbon additions via sensitivity studies within plausible ranges.

865   The effect on $\delta^{13}C_{carb}$ of a carbon addition of isotopic composition $\delta^{13}C_{carb}$ is given

866   approximately by mass-balance with the surface (atmosphere and ocean) carbon reservoirs

867   (*78, 79*). The effect on pH is additionally dependent on the rate of addition. We show in

868   Table S10 model results for combinations of addition size, isotopic composition and rate,

869   constrained to result in $\delta^{13}C_{carb}$ = -3 ‰, demonstrating the additional non-linear effect of

870   land-surface weathering feedbacks ('land carbonate compensation').

871   The decline in $\delta^{13}C_{carb}$ over the P-T boundary is faster than can be accounted for by

872   a decrease in land carbon burial alone, implying an additional pulse of isotopically light

873   carbon contribution ~-2‰ to the decline. We show in Figure S7 the constraints from the

874    $\delta^{11}B$ data on carbon additions over the 50kyr interval 251.95 − 251.90 Ma. The results

875   demonstrate that providing the rate of carbon addition is relatively slow as here, the pH

876 constraints are in fact relatively weak, and are consistent with a range of input isotopic

877 compositions $\delta^{13}C_{inj}$.

878 Table S10 Carbon injection perturbations, constrained to result in $\delta^{13}C_{carb}$ = -3 ‰ when
879 applied to steady-state condition CO_2Lo

Size (mol C)	Duration	Rate (mol / yr)	$\delta^{13}C_{inj}$	Δ pH
4.75×10^{17}	10^5 yr	4.75×10^{12}	-50	-0.07
2.47×10^{18}	10^5 yr	2.47×10^{13}	-10	-0.28
3.32×10^{17}	10^4 yr	3.32×10^{13}	-50	-0.18
1.75×10^{18}	10^4 yr	1.75×10^{14}	-10	-0.64

880

881 The acidification event at ~251.89Ma requires a rapid addition of carbon on a timescale ≤

882 10 kyr, with an isotopic composition $\delta^{13}C_{inj} \approx 0$ ‰ in order to leave $\delta^{13}C_{carb}$ unaffected, and

883 size ≥ 2×10^{18} mol in order to produce a sufficient decline in pH and $\delta^{11}B$ (Figure S8).

884 Larger (or more rapid) carbon additions produce relatively little additional response in

885 ocean pH, as the majority of the input carbon remains in the atmosphere, and the response

886 of the $\delta^{11}B$ is also non-linear at low pH. The rate of the inferred carbon addition is ~3 times

887 the estimates above for organic carbon from the combined effects of sills ($0.16 - 0.4 \times 10^{18}$

888 mol C over 10 kyr) and pipes ($0.1 - 0.3 \times 10^{18}$ mol C over ~6.5 kyr), but is not unreasonable

889 given the carbonate carbon source and large uncertainties in these estimates.

890

891 *6.2.5 SO₂ injection perturbation*

892 Contact metamorphism of evaporites resulting in large SO_2 release could potentially also

893 contribute to the acidification event. Quantitatively the effect (per mol) on ocean pH is

894   approximately twice that of a carbon addition, and given the relative abundance of

895   evaporites to carbonates is therefore likely to represent a smaller contribution to
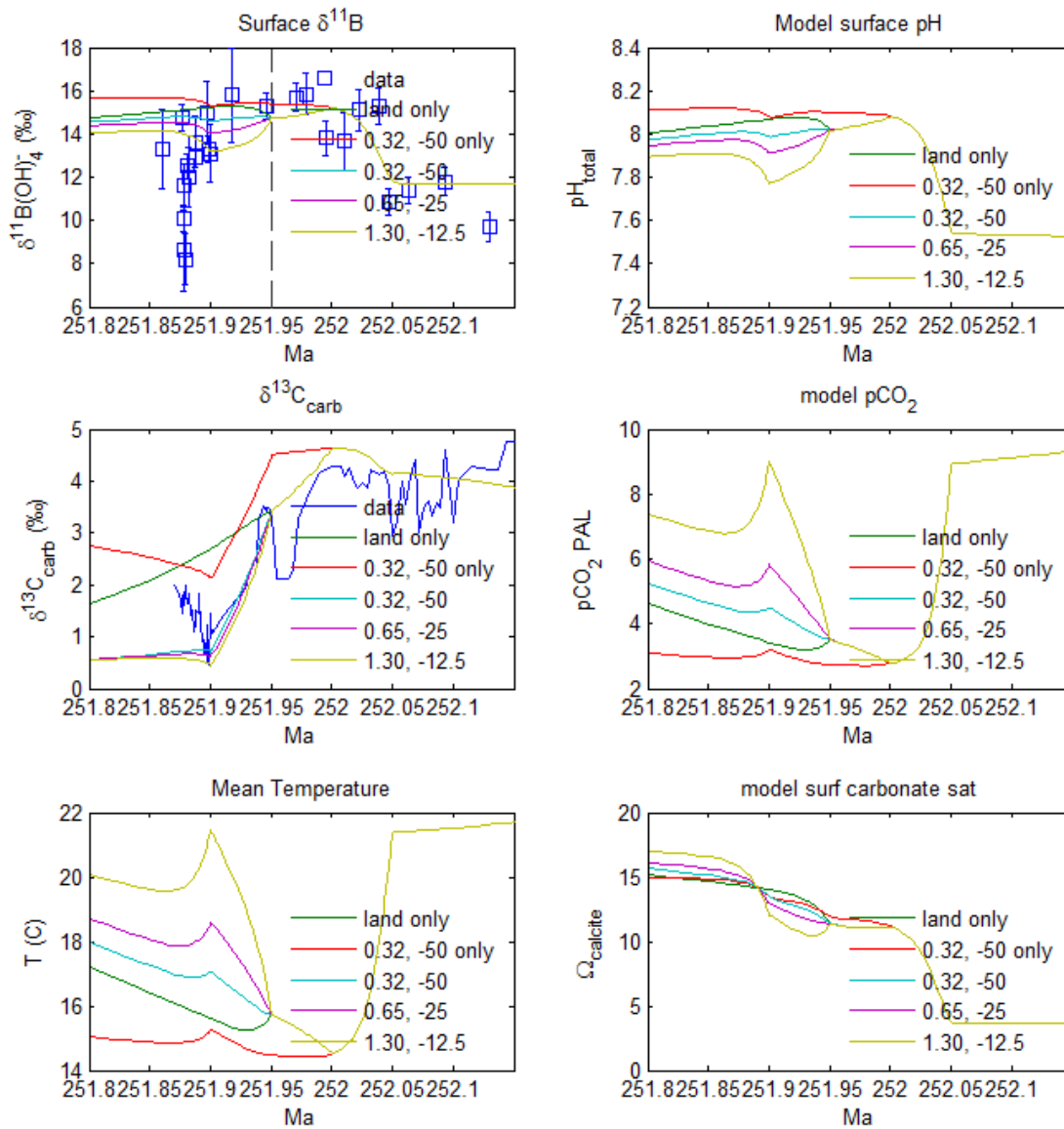
896   acidification.

Figure S7 Effect of changing size and isotopic composition of CO_2 input perturbations applied to scenario CO_2Hi over 50kyr interval 251.95 – 251.90 Ma. 'land only' shows the effect of interruption in land organic burial,'0.32. -50 only' shows the effect of carbon addition only. Other lines show combined effect of land burial and carbon addition. Perturbations are constructed to result in $\delta^{13}C_{carb} \approx$ -2 ‰, and correspond to inputs of: 0.32x10^{18} mol / -50 ‰; 0.65x10^{18} mol / -25 ‰; 1.30x10^{18} mol / -12.5 ‰
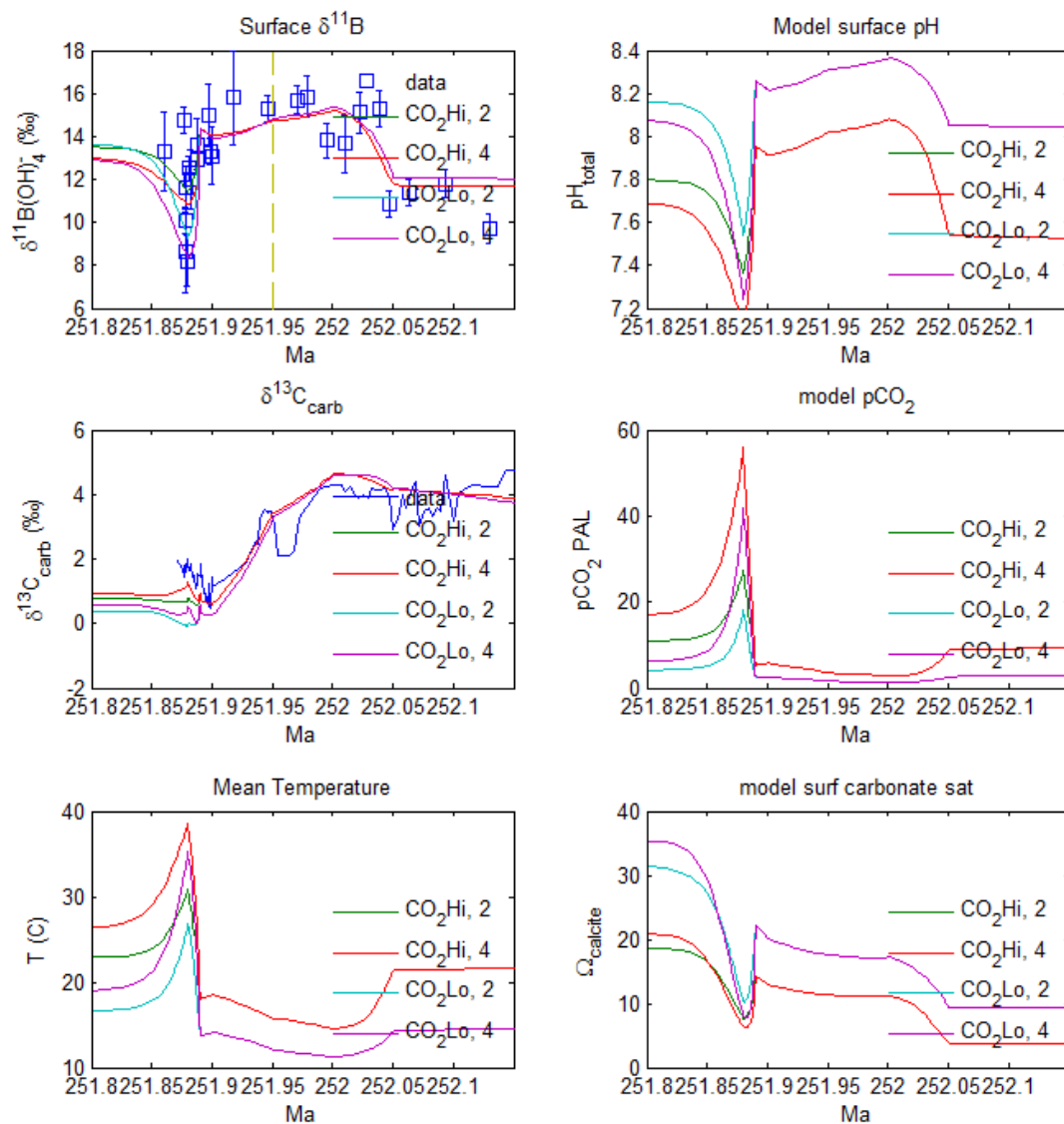
Figure S8 Effect of changing size of CO_2 input perturbations applied to scenarios *CO2Hi* and *CO2Lo* over 10kyr interval 251.89 – 251.88 Ma. Perturbation sizes are 2×10^{18} mol and 4×10^{18} mol. Isotopic composition is 2.65 ‰, ie equal to that of sedimentary carbonate.
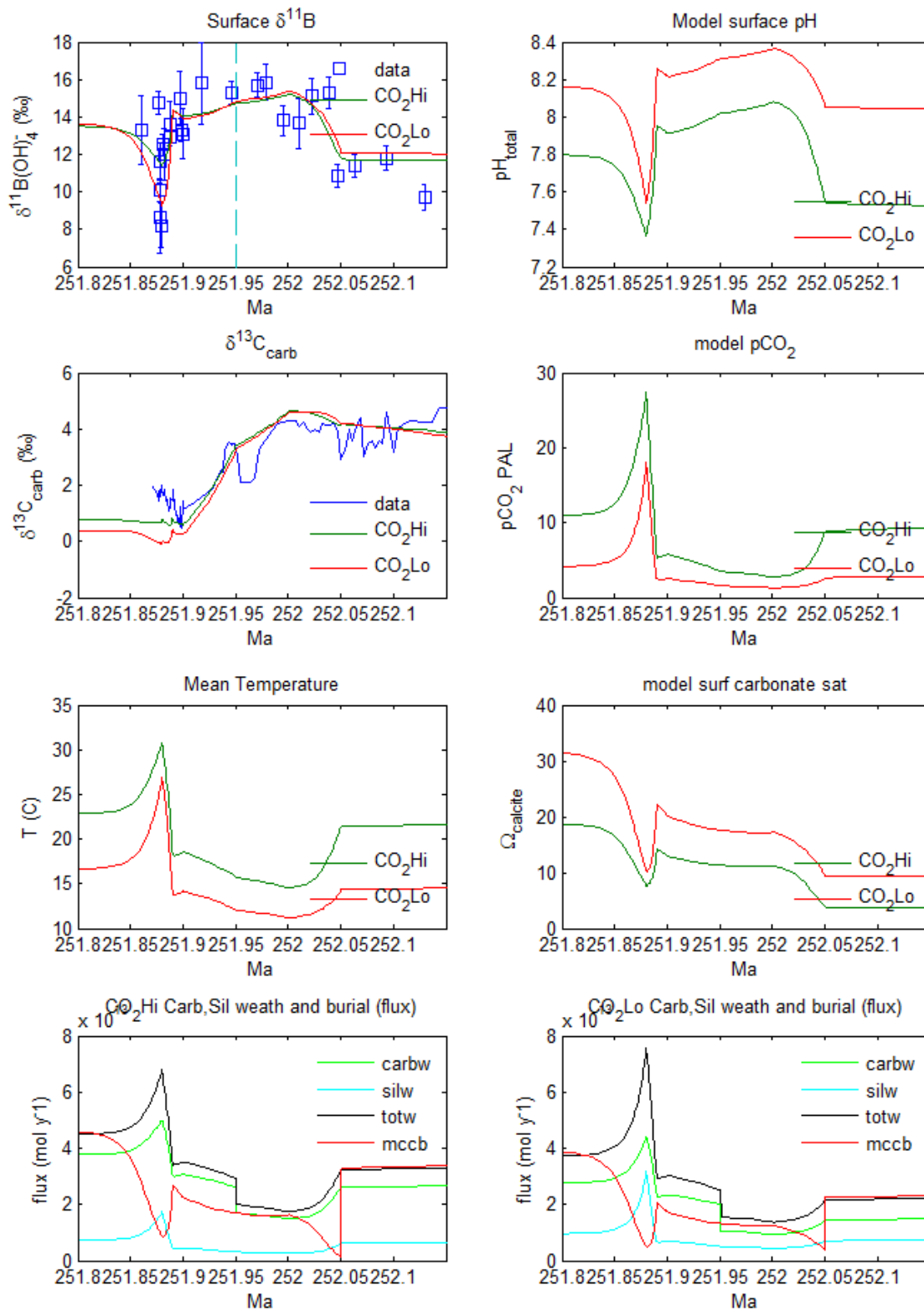
Figure S9 Additional model output for CO₂ scenarios shown in main paper Figure 3. Weathering fluxes are shown for scenario CO₂Lo only.

899